University of Alberta

Fluorescent-Core Microcapillaries: Detection Limits for Biosensing Applications

by

Shalon A. McFarlane

A thesis submitted to the Faculty of Graduate Studies and Research in partial fulfillment of the requirements for the degree of

Master of Science

Department of Physics

Spring 2013
Edmonton, Alberta

Abstract

This work develops a refractive-index sensor based on whispering gallery modes (WGMs) in glass microcapillaries. The capillary channel is coated with a layer of fluorescent silicon quantum dots (QDs), which provides a fluorescence source that also supports the WGMs. When different fluids are pumped into the channel, the fluorescence spectrum responds as the resonances shift to different frequencies. A study of the WGM spectral shift analysis techniques improved the detection limits to $\sim 10^{-4}$ refractive index units, and permitted the development of sensorgram-type analyses in which the channel fluid is probed continuously in time. The feasibility of the device as a microfluidic biosensor was demonstrated by first functionalizing the silica surface and then detecting the binding of biotin and streptavidin to the capillary channel. These structures could be attractive as microfluidic biological sensors, since they are easy to fabricate, mechanically robust, and relatively inexpensive compared to other technologies.

Acknowledgements

To quote Douglas Adams: "I may not have gone where I intended to go, but I think I have ended up where I needed to be." Nonetheless, I would not be where I am without the help of several individuals who have contributed in one way or another to my experience at the University of Alberta.

First and foremost, I would like to thank my supervisor, Dr. Al Meldrum. You have been a big influence on my academic life. You encouraged me to enter the Masters program and have been helpful and patient throughout the entire process. This thesis would not have been completed or written without your help. I cannot express how grateful I am for your guidance, knowledge and wisdom. Also, I appreciate how many times our conversations ended up in fits of laughter.

Next, I would like to thank both past and present members of the Meldrum group including Ross Lockwood, Kyle Manchee, Yanyan Zhi, Josh Silverstone, Zhihong Zhang, Stephen Lane, Torrey Thiessen, Kevin van der Meij, Teresa Sokolowski, Dr. Vanessa Zamora and Dr. Pablo Bianucci. I have thoroughly enjoyed coming into the lab every day for the past three and a half years and having you as my colleagues. You have taught me so much and it has been a privilege to learn from each one of you. A very special thanks goes to Kyle for passing on his expertise and for always being willing to help out after he left, via text or email when problems arose. I would not have been able to complete this thesis without your help!

I would also like to thank our chemistry collaborator, Dr. Jon Veinot and his group, particularly Dr. Jose Rodriguez, Sarah Regli and Dr. Melanie Hoffman, for always being tolerant enough to help out a physicist with chemistry problems.

Thank you to the technicians, Don Mullin and Greg Popowich. Don, no matter what problem I had, you knew just how to fix it, or how to improvise something that would work. Thank you Greg for teaching me the ways of the TEM and coming to my aid whenever the TEM did something unexpected, even if it was something trivial.

To my friends both near and far who kept my spirits up and showed me a life outside of physics; whether it be by sending me ridiculous text messages, grabbing a coffee or a beer (or several), to see a movie, or to just hang out. In particular, I would like to thank Geraldine Gratton, Sarah Miles, Sonia Budac, Dayna Rowlett, Abigail Stevens, Tania Wood, Cara

Ellis, George Coomber and Steven Olsen. Thanks to Joe Losby for teaching me a great deal about experimental physics and life.

Mom and Dad, I would not be the person I am today without you. Thank you for the phone calls, the wonderful trips overseas and putting up with my "blonde" moments. No words can describe how much I appreciate your infinite support. My brother Liam, you are a huge inspiration and have taught me to never give up and always keep a sense of humour. Thank you for all the lunch-time Skype chats during the writing process; they helped keep my sanity!

Last, but most importantly, I would like to thank my awesome partner Rhys Chouinard. I would not have been able to finish both my degrees without your support, encouragement, physics knowledge and great patience at all times. I'm very lucky to have you in my life and I appreciate all that you have done.

Contents

List of Tables

List of Figures

List of Abbreviations

APS	(3-aminopropyl)-siloxane
APTES	(3-aminopropyl)-triethoxysilane
APTMS	(3-aminopropyl)-trimethoxysilane
BSA	Bovine Serum Albumin
CCD	charge-coupled device
CF	curve fitting
DL	detection limit
EM	electromagnetic
FCM	fluorescent-core microcapillary
FOx	flowable oxide
FSR	free spectral range
FT	Fourier transform
FWHM	full-width half-maximum
HF	hydrofluoric acid
ID	inner diameter
IPA	isopropyl alcohol
IUPAC	International Unions of Pure and Applied Chemistry
LCORR	liquid-core optical ring resonator
LoC	lab-on-chip
MIBK	methyl isobutyl ketone
OD	outer diameter
PBS	phosphate buffer saline
PE	polyethylene
PL	photoluminescence

PMT	photomultiplier tube
PP	peak picking
QD	quantum dot
RIU	refractive index units
SA	streptavidin
SBIG	Santa Barbara Instrument Group
SEM	scanning electron microscope
SGS	self guided spectrograph
Si	silicon
SNR	signal-to-noise
SP	surface plasmon
SPR	surface plasmon resonance
TE	transverse electric
TEM	transmission electron microscope
TIR	total internal reflection
TM	transverse magnetic
VASE	variable angle spectroscopic ellipsometry
w/w	percent by weight
WGM	whispering gallery mode

List of Symbols

α	absorption coefficient
β_{sp}	SP propagation constant
$B_{\lambda,T}(\lambda)$	black body intensity
c	speed of light in vacuum $= 2.99792458 \times 10^8$ m/s
C	molar concentration
C_s	sucrose concentration
d	penetration depth
e	electronic charge $= 1.6022 \times 10^{-19}$ C
ε_0	permittivity of free space $= 8.85418782 \times 10^{-12}$ F/m
ε_M	complex dielectric of material
ε_r	relative permittivity of material
ε_S	complex dielectric of analyte
E_g	band gap energy
$\mathbf{E}$	electric field
η_R	quantum efficiency
f	frequency
Δf	FWHM or spectral linewidth
γ	Lorentzian linewidth
$\gamma(f)$	variable Lorentzian linewidth
$\hbar$	Planck constant $= 1.054571726(47) \times 10^{-34}$ J $\cdot$ s
I	intensity of field

$I(f)$	spectral lineshape
$I_{\lambda,T}(\lambda)$	Planck's law of blackbody radiation intensity
$J_l(z)$	Bessel function of the first kind
k, $\mathbf{k}$	wavenumber, wavevector
k_F	Fourier component
K_d	dissociation constant
l	WGM angular mode order
λ	wavelength
$\Delta\lambda_{min}$	resolution of measurement system
m	mass
μ	reduced mass $= (m_e^{-1} + m_h^{-1})^{-1}$
n	refractive index
N	number of points
Δn_{min}	detection limit (DL)
$\Delta\phi$	Fourier phase difference
ν	frequency
Q	quality factor
r	radius, or radial parameter
$r_{\perp,\parallel}$	reflection coefficient
ρ	WGM radial mode number
$R_{\perp,\parallel}$	power reflection coefficient
R_0	quantum dot radius
$S(\lambda),\ S(f),\ s(\lambda)$	spectral intensity
σ	standard deviation
$t_{\perp,\parallel}$	transmission coefficient
T	temperature
$T_{\perp,\parallel}$	power transmission coefficient
τ	photon lifetime or energy damping time
τ_{NR}	non-radiative decay lifetime

τ_R	radiative decay lifetime
θ_c	total internal reflection critical angle
θ_{sp}	resonance angle for SPs
v	phase velocity
V_{TE}	potential
ω	angular frequency
$Y_l(z)$	Bessel function of the second kind

Chapter 1

Introduction: Biomolecule detection using microscale sensors

1.1 The need for biological sensors

The International Union of Pure and Applied Chemistry (IUPAC) defines a biosensor as "a device that uses specific biochemical reactions mediated by isolated enzymes, immunosystems, tissues, organelles or whole cells to detect chemical compounds, usually by electrical, thermal or optical signals" [1]. In a broader sense, a biosensor is a device that can analyze biomolecular interactions under controlled conditions. However, based on the IUPAC definition, the target analyte itself does not necessarily need to be biological. This allows for a wider range of biosensor applications: diagnostic tools for disease in medicine, aid in drug discovery and pharmaceutical research, environmental detection of contaminants (pesticides, oil) in river/ground water, homeland security, or the discovery of drug residues (such as antibiotics) in food or urine [2–6].

One of the most well-known and successful biosensors monitors blood glucose levels in diabetic patients.[1] Only a drop of blood is needed and the device can read out a reliable blood glucose concentration in seconds. The sensing mechanism is

[1]The other well-known commercially available biosensors are for home pregnancy and ovulation tests.

based on the Clark electrode method used to measure oxygen levels in blood [7]. This was also one of first commercially available biosensing devices, and research is still being done to further improve the sensor in order to miniaturize it, decrease the detection time, or even to implant a wireless device into the body [8]. The glucose sensor is a model for the development of practical devices for the rapid and reliable detection of other biomolecules, and for diagnosing diseases such as cancer or pathogenic viruses [9]. Ideally biosensors should be highly sensitive to a specific target analyte and produce reliable[2] results in the shortest amount of time. For many applications, they should be stable, inexpensive, portable, and easy to use [1, 3].

Biological sensors involve molecular interactions on the nanometer scale. Intuitive candidates for biosensing devices include nanomaterials and nanotechnology. Miniaturizing these sensors may also increase the sensitivity as well by allowing for a small analyte volume or sample size [3]. The size, shape, and surface chemistry of nanoparticles can be controlled and optimized, leading to tunable chemical and physical properties. The reduced sizes for nanotechnology-based sensors may assist in the development of lab-on-a-chip (LoC) technologies, specifically utilizing microfluidic systems [3, 4, 9, 10].

1.1.1 Biosensor elements

There are three main elements of a biosensor: a recognition site, a transducer, and an amplifier (Figure 1.1) [1,3,5]. The sensor head itself is comprised of a recognition site and a transducer. The recognition site is a surface or volume that is sensitive to the analyte of interest and involves a bioelement or bioreceptor. This element could be in the form of a receptor, an enzyme, an antibody, a nucleic acid, or an ion channel designed to specifically interact with, and only with, the molecule of interest [4,5,9]. The transducer is the specific mechanism of detection; it transforms the interaction of the sensing element and the analyte into a quantifiable signal. This detection signal can take many different forms but can be divided into four main

[2] *i.e.*, have minimal likelihood of *false positive* or *false negative* results [1].

transducer mechanisms: electrical, thermal, mechanical, and optical[3] [2, 11]. This signal is communicated to the amplifier where it is amplified and displayed, ideally in a user friendly way [3–5]. The type of element chosen and designed is dependent on the desired usage, and each type has its own set of advantages and disadvantages.

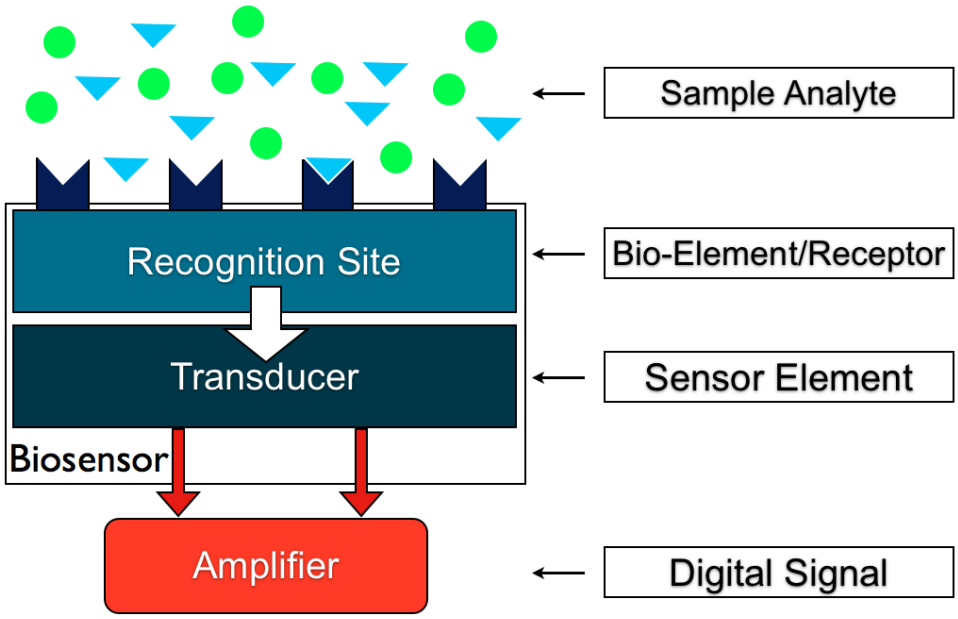

Figure 1.1 – General schematic of a biosensor. Adapted from Refs. [3] and [5].

1.2 Optical biosensors

There are many different methods by which a biosensor can detect the presence of an analyte. Optical sensing methods, in particular, permit rapid analysis for real time detection. An advantage of optical sensors over other transducer mechanisms is the capability for probing the analyte in a nondestructive manner, allowing for *in situ* sensing. Optical methods can also give a high signal-to-noise ratio (SNR) and involve relatively simple designs compared to other transducer types [9, 12]. Optical signals are immune to electromagnetic interference and are capable of remote sensing (*i.e.*, the transducer does not need to be directly connected to the amplifier) [3, 12]. The signals can then be analyzed using a charge-coupled device (CCD) detector.

[3]Each category can be further subdivided into groups including electrochemical, electromechanical, and piezoelectric sensors, etc.

Versatile optical sensors are ones that are not limited by the type of light source used [11].

Optical detection methods can be classified according to whether or not the analyte must be labelled. The most common type of labelled detection uses a fluorescent molecule or dye to tag the target analyte. Fluorescent molecules include organic fluorophores or dyes such as "Green Fluorescent Protein". When the fluorescent label is excited by an external light source, its fluorescence indicates the presence of the analyte. Combined with appropriate surface functionalization chemistry, this method can be used to sense single target molecules [9, 13].

However, there are some major chemical and physical limitations associated with labelled detection. First, fluorescence quenching or bleaching can reduce the signal intensity, leading to a less sensitive detection system [2,6,9]. Second, toxicity associated with the fluorescent marker can be a problem[4] and, third, fluorescent labeling of a target molecule can alter its binding properties [9,14]. Finally, naturally occurring fluorescence in biological molecules, called cell autofluorescence, can also mask the signal and lead to false positives.

In label-free analysis, the target analyte is directly detected. Unlabelled detection occurs at the transducer site by measuring a change in the optical properties caused directly by the analyte molecules. Transduction methods include changes in absorbance, reflectance, or scattering, or they can be based on changes in the local refractive index. Figure 1.2 depicts a general schematic for label-free detection using optical methods. Label-free detection involves the immobilization of the target molecule on the surface. In these surface sensitive techniques, the interface between the sensor substrate and the recognition site[5] is illuminated, and the analyte is detected when the target molecule reacts with the recognition site, causing a change in the local optical properties that are sampled by the incident light. This interaction causes a detectable signal, which can be amplified and displayed. Examples of the optical signals that can be measured include intensity or reflection angle.

[4] Especially for *in vitro* imaging, and for the disposal of the fluorescent dye.

[5] Generally the recognition site is a biomolecule.

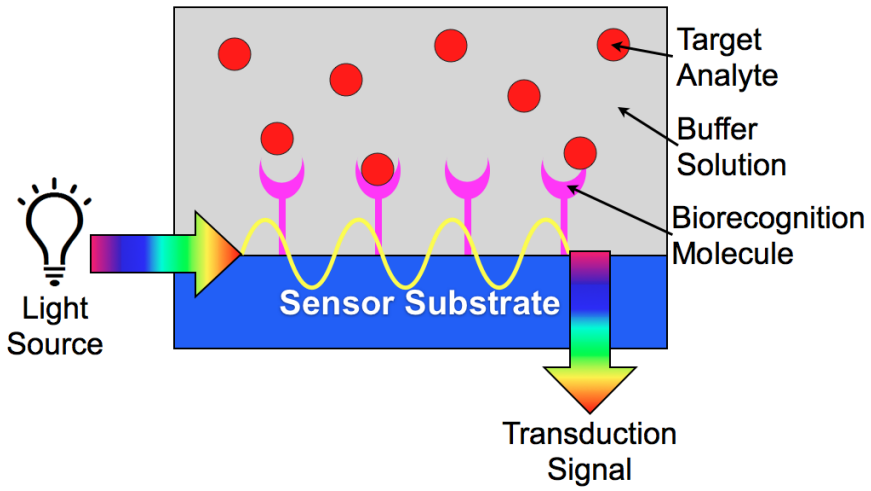

Figure 1.2 – Conceptual image of a label-free optical biosensor. A light source illuminates the sensor substrate and the transduction signal can be a change in refractive index, reflectance, absorbance, phase, or scattering signal. Modified from Ref. [12].

1.2.1 Sensors based on surface plasmon resonance

Since first demonstrated by Liedberg *et al.* in 1983 as a biosensor [15], surface plasmon resonances (SPR) have become arguably the most powerful transduction tool for the optical detection of biomolecules. SPRs are essentially the resonant oscillations of conduction electrons in a confined metallic structure such as a nanoparticle or thin film. Light incident on a metal-dielectric interface can excite surface plasmons (SPs) by interacting with the delocalized electrons in the metal film. When the momentum of the incoming photon matches that associated with the plasmon resonance, SP waves propagate parallel to a metal-dielectric interface (or a metal-vacuum interface) [16, 17].

The resonant frequency of the propagating SP waves is sensitive to the optical properties of the adjacent medium (the dielectric layer containing the analyte) and responds to changes in the local refractive index (Figure 1.3(a)). The SP evanescent wave penetration depth is roughly 100–500 nm at visible and near infrared wavelengths, so the sensing action takes place close to the metal-dielectric interface [16,18]. Since SPR-type sensors are among the most advanced optical biosensing methods, the basic physics will be described briefly herein. This may give an idea of the advantages and limitations of the method, and provide a point of comparison

for the current work.

1.2.1.1 Basic physics of SPR sensors

Surface plasmons are excited when a light source incident on the surface interacts with the free electrons in the metal layer, at a specific frequency, ω. Excitation of SP waves can only occur when the incident light is able to couple energy to the plasmon. Since the SP wave propagates along the interface, this can only occur with TM polarized incident light [1, 16, 19, 20].

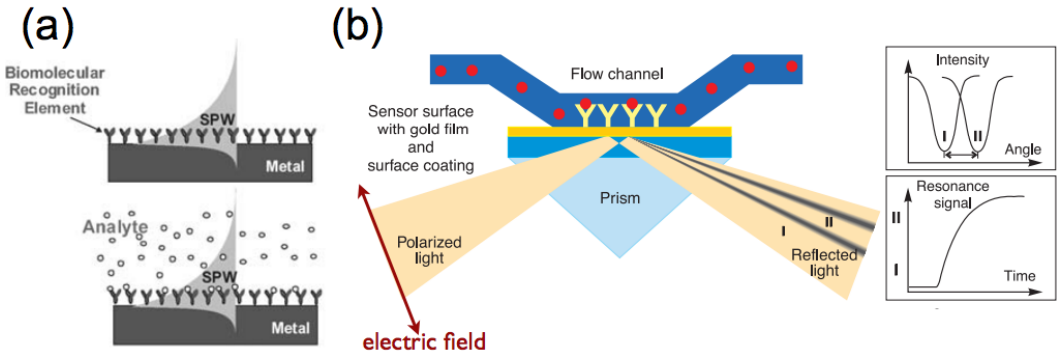

Figure 1.3 – Schematic of surface plasmon resonance. (a) Image showing SPR biosensing by the surface plasmon wave propagating along the interface. The SPW does not extend far into the sample dielectric. Reproduced from Ref. [16] (b) Schematic of the Kretschmann configuration for SPR biosensing. Polarized light is reflected from a gold film, and the change in resonance angle of the reflected light can be detected. Modified from Ref. [21].

Most commercially available devices use a prism coupling set-up referred to as the "Kretschmann geometry," shown in Figure 1.3(b). In this configuration a light source passes through a prism and reflects from the back of the sensor chip surface and into a CCD or a photomultiplier tube (PMT). At an incident angle (θ_{sp}) that satisfies the resonance condition (momentum matching of photons and plasmons), the incoming light creates plasmon oscillations [2, 22]. This angle is given by

$$\sin\theta_{sp} = \frac{1}{n_p}\sqrt{\frac{\varepsilon_M \varepsilon_S}{\varepsilon_M + \varepsilon_S}}, \tag{1.1}$$

in which n_p is the refractive index of the prism, $\varepsilon_M = n_M^2$ is the complex dielectric constant of the metal, and $\varepsilon_S = n_S^2$ is the dielectric constant of the analyte region.

The resulting TM-polarized SP wave propagates parallel to the metal-dielectric interface with a propagation constant, β_{sp}, given by

$$\beta_{sp} = \frac{\omega}{c}\sqrt{\frac{\varepsilon_M \varepsilon_S}{\varepsilon_M + \varepsilon_S}} = \frac{2\pi}{\lambda}\sqrt{\frac{\varepsilon_M \varepsilon_S}{\varepsilon_M + \varepsilon_S}}, \tag{1.2}$$

where ω is the angular frequency, c is the speed of light in vacuum, and λ is the free-space wavelength [20]. The resonant angle and propagation constant are related through

$$\sin\theta_{sp} = \frac{\beta_{sp}}{n_p}\frac{\lambda}{2\pi}. \tag{1.3}$$

Thus, the creation of a SP wave is dependent on the incident angle, the wavelength, the refractive index of the prism and the materials chosen for the metal and dielectric layer.

By applying the appropriate boundary conditions, the dispersion relation is given by

$$k_M \varepsilon_S + k_S \varepsilon_M = 0, \tag{1.4}$$

where k_M and k_S are transverse wavenumbers for the metal and dielectric region, respectively. Since $\varepsilon_S > 0$, Eq. (1.4) shows that ε_M must be negative [22]. In order for the propagation constant in Eq. (1.2) to be real, this also requires that the magnitudes of the dielectric constants are such that $|\varepsilon_S| < |\varepsilon_M|$ [16, 22]. Gold is commonly the metal of choice. In addition to meeting the above requirements, gold has further advantages that it does not oxidize and its surface chemistry is compatible with many types of surface functionalization procedures [18]. It also produces a strong SPR signal in the near-infrared[6] region which is important for discerning the signal from background noise, especially for low analyte concentrations [22].

There are several different ways that changes taking place on the sensor surface can be detected. In the Kretschmann set-up described above, light of a specific

[6]Other metals such as silver, copper, aluminum, titanium and chromium can exhibit SPR in the visible region of the spectrum.

wavelength is incident on the surface and scanned over a range of different angles. When the resonance condition in Eq. (1.3) is satisfied, *i.e.*, at a specific resonance angle, the creation of a surface plasmon results in an intensity drop in the reflected beam. This correlates to a minimum in a graph of reflected intensity *vs.* angle, as seen in the inset to Figure 1.3(b). The shape and central wavelength of this minimum can be translated into information about the sensor surface. For example, a biomolecular interaction on the surface changes the local refractive index, causing the SP resonance to occur at a different resonance angle, as shown in Eqns. (1.1)–(1.3). Alternatively, if a fixed angle is used, one can scan the incident wavelength in order to find the plasmon resonance for that angle [16, 20]. Also, by monitoring the SPR response over time, as shown in the lower inset to Figure 1.3, information can be gained about the kinetic behaviour of binding events.

SPR sensing was the basis of the first commercially available, real-time optical bioanalysis tool, which was initially developed in 1990 by the company BIAcore (initial company Pharmacia Biosensor) [1,23,24]. Other commercially available SPR sensors include the Spreeta from the Texas Instruments Group [25] and the Kinetic Instruments 1 developed by BioTuL Bio Instruments GmbH [26]. These devices have detection limits approaching 10^{-6} refractive index units (RIU), meaning that changes in the refractive index as small as one part in a million can be detected [16]. Commercially available devices have also demonstrated real-time analysis on timescales as short as 0.1 seconds [27].

Despite these attractive properties, however, there are also several drawbacks associated with commercial SPR-based sensors. One of the most significant is the high up-front instrument cost [9,20]. Some commercial instruments cost US$150,000 to $300,000, not including supplies [27, 28]. The signal-to-noise (SNR) ratio can be low, and the limited interaction length of the SP wave with the analyte can lead to a corresponding limited sensitivity [17]. Finally, these commercial devices are large-scale analysis methods based on bulky prisms and light sources, so they are incompatible with LoC-based systems. Therefore, much work is currently being done to miniaturize SPR-based optical sensors [16].

1.2.2 Sensors based on optical microcavities

Sensors based on optical microcavities may be able to address some of these issues. Photons can traverse a microcavity numerous times, thereby increasing the effective interaction length and ultimately the sensitivity of the device. There are many different types of microresonators which are available in a myriad of structures and geometries, each with certain advantages with respect to sensing applications. Thus, some description of the key microcavity parameters is necessary.

The optical quality factor (Q-factor) is a measure of the rate at which electromagnetic (EM) energy is lost from the cavity. The Q-factor is related to the number of oscillations required for the field in the cavity to decay by a factor of $1/e$ of its original value. The definition of the Q-factor is

$$Q = 2\pi \frac{\text{energy stored}}{\text{energy dissipated per cycle}}. \tag{1.5}$$

An alternative, but equivalent definition (as long as Q is not too low) relates the Q-factor to the resonance linewidth:

$$Q = \frac{f_0}{\Delta f} = \frac{\lambda}{\Delta\lambda}, \tag{1.6}$$

where f_0 is the resonant frequency of the cavity, and Δf is the full-width half-maximum (FWHM) of the resonance or the spectral line width [29]. The Q-factor can also be defined in terms of the photon lifetime (or the energy damping time) $\tau = Q/\omega$.

The overall cavity Q-factor is controlled by the various loss mechanisms:

$$Q^{-1} = Q_{\text{rad}}^{-1} + Q_{\text{scat}}^{-1} + Q_{\text{mat}}^{-1} + \sum_i Q_i^{-1}, \tag{1.7}$$

where Q_{rad} represents the Q-factor due only to diffractive losses due to surface curvature, Q_{scat} represents the Q-factor associated with scatting losses due to surface inhomegeneities, Q_{mat} is from material losses such as absorption, and $\sum_i Q_i^{-1}$ corresponds to the limiting Q-factors associated with any other loss mechanisms. In a

smooth, clean, and perfectly spherical microcavity, the principal loss is typically due to absorption. Accordingly, the limiting Q-factor is given by

$$Q = \frac{2\pi n}{\alpha\lambda}, \tag{1.8}$$

where α is the material's absorption coefficient and n is its index of refraction. In the best cases, Q-factors in optical microspheres can have values as high as 10^{10} [30]. With an absorbing or scattering surface layer, Q-factors are typically in the range of 10^3–10^9 [31–36].

Optical cavities that exhibit the so-called whispering gallery mode (WGM) resonances are of particular interest in this work. In spherical or cylindrical optical microcavities, light travels around the periphery of the cavity via total internal reflection (TIR), which increases the interaction length of the evanescent field with the analyte by a factor proportional to Q. WGMs will be the basis of a sensor studied in this thesis, therefore some description of their properties will be provided in the following paragraphs.

1.3 Whispering Gallery Mode sensors

Optical whispering gallery modes are named after their acoustic counterparts, which were initially studied in St. Paul's cathedral in London and explained theoretically by Lord Rayleigh in 1910 [37]. If two people stand on opposite sides of the so-called "Whispering Gallery" (a dome with a diameter of ∼32 m), a whisper on one side can be heard clearly at the other. This is because sound reflects off the curved walls of the gallery with relatively little loss, forming an acoustic standing wave at particular resonances. The same concept can be applied to light inside optical microcavities, specifically those with spherical or cylindrical geometries.

1.3.1 Total internal reflection and the evanescent wave: basics

When light travels across an interface from one dielectric medium to the next, part of the wave is reflected and part is refracted, as shown in Figure 1.4(a). The magnitude

of the reflected and transmitted amplitudes are described by the well known Fresnel Equations:

$$r_\perp = \frac{E_{r\perp}}{E_{0\perp}} = \frac{n_i \cos\theta_i - n_t \cos\theta_t}{n_i \cos\theta_i + n_t \cos\theta_t}, \quad t_\perp = \frac{E_{t\perp}}{E_{0\perp}} = 1 + r_\perp \tag{1.9}$$

$$r_\parallel = \frac{E_{r\parallel}}{E_{0\parallel}} = \frac{n_t \cos\theta_i - n_i \cos\theta_t}{n_i \cos\theta_t + n_i \cos\theta_i}, \quad t_\parallel = \frac{E_{t\parallel}}{E_{0\parallel}} = (1 + r_\parallel)\frac{\cos\theta_i}{\cos\theta_t} \tag{1.10}$$

$$R = |r|^2 \tag{1.11}$$

$$T = 1 - R, \tag{1.12}$$

where n_i is the refractive index of the incident medium, n_t is the index of the transmitted medium, θ_i is the incident angle, θ_t is the transmitted angle, and r and t are the reflection and transmission coefficients, respectively [29,38–41]. R and T are the reflectance and transmittance, *i.e.*, the fraction of optical power in the incident wave that is reflected or transmitted. For the transverse electric (TE) polarization, the electric field is perpendicular to the plane of incidence, and vice-versa for the transverse magnetic (TM) polarization.

The angles of incidence and refraction are related via Snell's Law. For angles of incidence above the critical angle, θ_c, the Fresnel Equations (Eqns. (1.9)–(1.12)) reveal that the entire wave is reflected, *i.e.*, $R_i = 1$ and $T_i = 0$ (Figure 1.4(b)). However, according to Maxwell's equations, the EM field cannot abruptly go to zero at the boundary. In accordance with the continuity of the fields, an "evanescent wave" must propagate along the dielectric boundary. Its intensity, I, decays exponentially as a function of distance z from the interface:

$$I = I_0 \exp(-z/d), \tag{1.13}$$

where d is the penetration depth of the evanescent wave. How far the field extends into the low-index medium depends on the refractive indices of the two media:

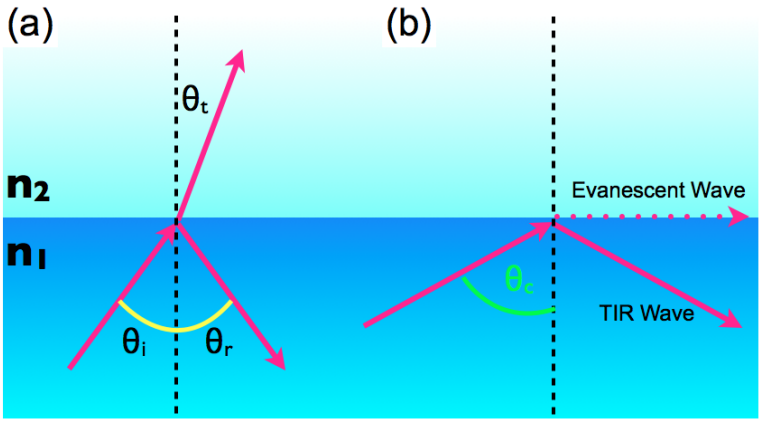

Figure 1.4 – Schematic of total internal reflection. The incident wave is traveling from a lower index to a higher index medium ($n_1 > n_2$). (a) A wave is both transmitted (refracted) and reflected. (b) Total internal reflection occurs when the incident angle is equal to or above a critial angle.

$$d = \frac{\lambda}{2\pi n_1} \frac{1}{\sqrt{\sin^2\theta_i - \sin^2\theta_c}} = \frac{\lambda}{2\pi} \frac{1}{\sqrt{n_1^2 \sin^2\theta_i - n_2^2}}. \tag{1.14}$$

This evanescent wave is important in optical microresonators and can be used for a number of applications. It is the mechanism for coupling light into a microcavity and, as with SPR sensors, it is the means by which the field can "sample" the external surroundings.

The penetration depth is dependent on the refractive indices of both media. Although these calculations are for a flat film (for a glass-air interface), they produce an estimation of how far the WGMs extend into the outside medium. If the incident angle is 45° and the wavelength is 800 nm, the penetration depth is ∼550 nm. This value decreases for larger angles of incidence and is typical of the evanescent distance associated with the WGMs. Thus, larger WGM cavities, which support nearly surface-parallel rays (Figure 1.5), have a smaller evanescent wave extension into the environment.

1.3.2 A brief description of the whispering gallery modes

In optical microresonators, whispering gallery modes develop near the interface of the cavity and the external medium, because of total internal reflection at the boundary

(Figure 1.5). In cylinders, the WGMs can be equatorial or spiraling, whereas in spheres they can include a polar configuration as well. Since this work uses the equatorial WGMs of a cylinder, we will focus on the equatorial modes specifically.

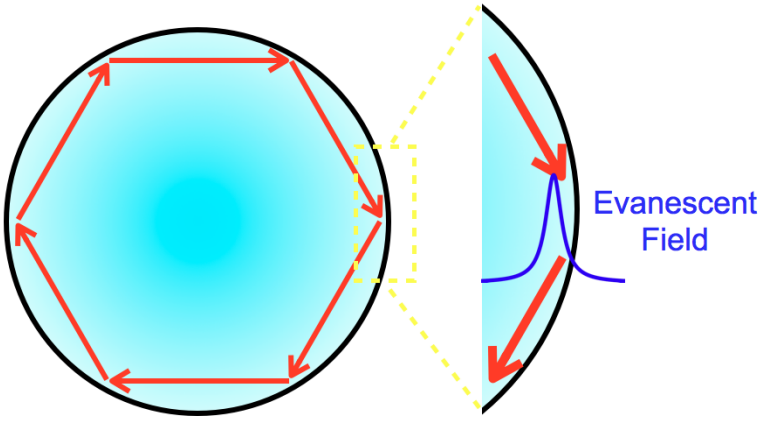

Figure 1.5 – Total internal reflection in optical microcavities. Inset shows the evanescent field of the whispering gallery wave between the resonator wall/medium interface.

Equatorial WGMs can be described by two main mode numbers: the angular mode order, l, defined as the number of wavelengths in the azimuthal direction, and the radial mode number, ρ, which is the number of intensity maxima in the radial direction. In the simplest picture, WGMs can be described using a trivial geometric analysis:

$$\lambda_l = \frac{2\pi r n}{l}, \tag{1.15}$$

where λ_l, the resonant wavelength, for any mode order l, can be determined as a function of the resonator radius, r and its refractive index, n.

However, the ray model of Eq. (1.15) fails to fully describe the WGMs, since it neglects a complete picture of the field amplitude of an open resonator. In order to get a correct description of the light inside the cavity, the resonances must be determined by writing Maxwell's equations in the specific geometrical coordinate systems and solving them numerically using appropriate boundary conditions.

1.3.2.1 WGMs in a sphere

The WGMs can be most easily understood in the case of a microsphere, which is the simplest geometry [36, 42, 43]. Consider a sphere in polar coordinates (r, θ, ϕ) with a radius a. The refractive index can be defined as a function of the radial distance

$$n(r) = \begin{cases} n_1 & \text{if } r < a \\ n_2 & \text{if } r > a, \end{cases} \tag{1.16}$$

where $n_2 > n_1$ (Figure 1.6(a)). The electric field amplitude associated with the resonances of the sphere can be solved using the vector Helmholtz equation in spherical coordinates:

$$\nabla^2 \mathbf{E} - k^2 n^2(r) \mathbf{E} = 0. \tag{1.17}$$

Teraoka and Arnold [42, 44] showed that the solution to Eq. (1.17) can be simplified by the introduction of a scalar function, $S_l(r, k)$, describing the magnitude of the field as a function of r and k, yielding

$$\left[-\frac{\partial^2}{\partial r^2} + V_{TE}(r, k) + \frac{l(l+1)}{r^2} \right] S_l(r, k) = k^2 S_l(r, k), \tag{1.18}$$

in which the potential is

$$V_{TE}(r, k) = k^2 [1 - n^2(r)]. \tag{1.19}$$

A solution to Eqns. (1.16)–(1.19) can be obtained using spherical Bessel functions:

$$S_l(r, k) = \begin{cases} A\psi_l(n_1 kr) & \text{if } r < a \\ C\psi_l(n_2 kr) + D\chi_l(n_2 kr) & \text{if } r > a, \end{cases} \tag{1.20}$$

where $\psi_l(z) \equiv z J_l(z)$, $J_l(z)$ is the order l spherical Bessel function of the first kind, $\chi_l(z) \equiv z Y_l(z)$, $Y_l(z)$ is the order l spherical Bessel function of the second kind, and A, C and D are proportionality constants.

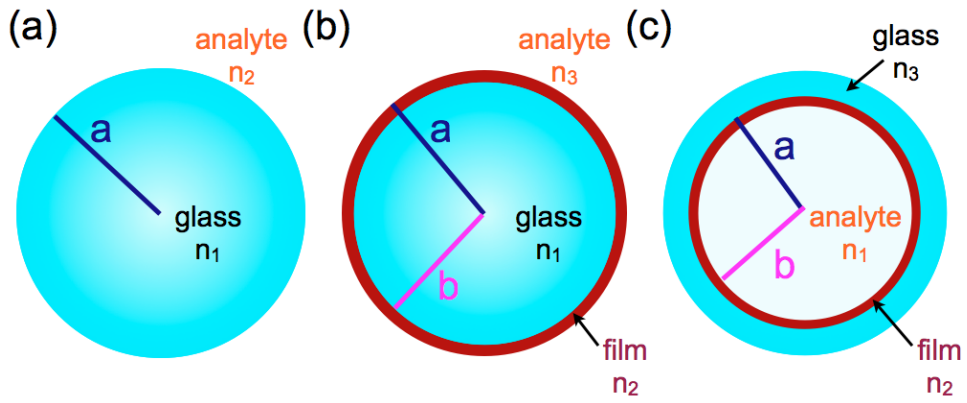

Figure 1.6 – Three optical resonators with circular cross sections (a) An uncoated sphere, (b) A coated sphere, and (c) A channel-coated capillary. For the first two cases the analyte is external to the structure, while in (c) it is located in the inner channel.

In order to solve Eq. (1.20) for the field amplitude of a given WGM, the boundary conditions are established at the sphere-medium interface. Accordingly, for the TE polarization, the electric field and its derivative must be continuous across the interface. From Eq. (1.20), this condition yields

$$n_1 \frac{\psi_l'(n_1 k_0 a)}{\psi_l(n_1 k_0 a)} = n_2 \frac{\chi_l'(n_2 k_0 a)}{\chi_l(n_2 k_0 a)}, \tag{1.21}$$

where the prime denotes the derivative with respect to the argument. The roots of this equation, k_0, can be solved numerically for any mode order l, using standard mathematical software packages. Eq. (1.21) has an infinite number of solutions, *i.e.*, there are an infinite number of possible radial orders for given mode order, l. The resonance of the TM mode can be solved algebraically using a similar method, with the appropriate boundary conditions:

$$\frac{1}{n_1} \frac{\psi_l'(n_1 k_0 a)}{\psi_l(n_1 k_0 a)} = \frac{1}{n_2} \frac{\chi_l'(n_2 k_0 a)}{\chi_l(n_2 k_0 a)}. \tag{1.22}$$

1.3.2.2 WGMs in a coated sphere

The resonances in a sphere coated with a layer having a different refractive index can be treated similarly [45, 46]. The derivation is more complicated in this case but the solutions are similar to those for the uncoated sphere in the previous section.

For a coated sphere, the radial refractive index profile is

$$n(r) = \begin{cases} n_1 & \text{if } r < b \\ n_2 & \text{if } b < r < a \\ n_3 & \text{if } r > a, \end{cases} \tag{1.23}$$

in which b is the radius of the sphere and a is the distance from the centre of the sphere to the outer edge of the coating (Figure 1.6(b)). Thus, $a - b$ is the thickness of the coating. The variables n_1, n_2, and n_3 are the refractive index of the sphere, film, and outside medium, respectively. Following a similar derivation as for the case of a simple sphere [45], the TE resonances are described by

$$S_l(r,k) = \begin{cases} A\psi_l(n_1 kr), & \text{if } r < a \\ C\psi_l(n_2 kr) + D\chi_l(n_2 kr) & \text{if } b > r > a \\ B\chi_l(n_3 kr), & \text{if } r > b, \end{cases} \tag{1.24}$$

where A, B, C, and D are constants. The solutions for TE modes are, again, established via the boundary conditions [45, 46]:

$$\frac{n_2\chi_l'(n_2 ka)}{n_3\chi_l(n_2 ka)} = \frac{(C_l/D_l)\psi_l'(n_2 ka) + \chi_l'(n_2 ka)}{(C_l/D_l)\psi_l(n_2 ka) + \chi_l(n_2 ka)}, \tag{1.25}$$

where

$$\frac{C_l}{D_l} = \frac{n_2\psi_l(n_1 kb)\chi'(n_2 kb) - n_1\psi_l'(n_1 kb)\chi_l(n_2 kb)}{-n_2\psi_l(n_1 kb)\psi'(n_2 kb) + n_1\psi_l'(n_1 kb)\psi_l(n_2 kb)}. \tag{1.26}$$

The TM modes have an analogous solution.

1.3.2.3 WGMs in a cylinder

The derivation for the WGMs in a coated cylinder is similar to that for a coated sphere. Cylinders are more relevant to this thesis, since the experimental structure to be described in Sect. 1.4.2 has a coating on the inner channel of a thick-walled capillary. The coated cylindrical structure can also be defined by Eq. (1.24), where

in this case, b is the distance from the centre of the capillary to the inner boundary of the coating and a is the inner radius of the capillary. Thus $a - b$ again represents the film thickness. Here, n_1 is the analyte index (the inner channel in the capillary), n_2 is the index of the film or coating, and n_3 is the index of the glass capillary wall (Figure 1.6(c)).

Accordingly, the WGMs can be solved for the TE polarization:

$$\frac{n_3 Y_l'(n_3 ka)}{n_2 Y_l(n_3 ka)} = \frac{(C_l/D_l)J_l'(n_2 ka) + Y_l'(n_2 ka)}{(C_l/D_l)J_l(n_2 ka) + Y_l(n_2 ka)}, \tag{1.27}$$

where

$$\frac{C_l}{D_l} = \frac{n_2 J_l(n_1 kb)Y_l'(n_2 kb) - n_1 J_l'(n_1 kb)Y_l(n_2 kb)}{-n_2 J_l(n_1 kb)J_l'(n_2 kb) + n_1 J_l'(n_1 kb)J_l(n_2 kb)}. \tag{1.28}$$

Similarly, the solutions for TM polarization are

$$\frac{n_2 Y_l'(n_3 ka)}{n_3 Y_l(n_3 ka)} = \frac{(C_l/D_l)J_l'(n_2 ka) + Y_l'(n_2 ka)}{(C_l/D_l)J_l(n_2 ka) + Y_l(n_2 ka)}, \tag{1.29}$$

where

$$\frac{C_l}{D_l} = \frac{n_1 J_l(n_1 kb)Y_l'(n_2 kb) - n_2 J_l'(n_1 kb)Y_l(n_2 kb)}{-n_1 J_l(n_1 kb)J_l'(n_2 kb) + n_2 J_l'(n_1 kb)J_l(n_2 kb)}. \tag{1.30}$$

Here, $J_l(z)$ is the order l cylindrical Bessel function of the first kind, and $Y_l(z)$ is the order l cylindrical Bessel function of the second kind.

1.4 Refractometric sensing with microcapillaries

Whispering gallery modes can be employed as refractometic sensors in optical microcavities. By numerically solving Eqns. (1.27)–(1.30), the whispering gallery mode electric field profile can be plotted. Accordingly, Figure 1.7 illustrates the TE-polarized first- and second-order radial modes for a coated capillary. The tail of the WGM extends into the capillary channel, "sensing", or interacting with the channel medium. By changing the refractive index of the medium (either in bulk or by at-

taching a molecule to the film surface) a shift in the resonance frequency will occur. As shown in Figure 1.7, the WGM profile for the first-order radial mode typically does not extend as far into the channel as that for the second order modes. Thus, some of the highest reported sensitivities are for the 2nd radial order modes (and even 3rd order) of liquid core optical ring resonators (LCORRs) [47, 48].

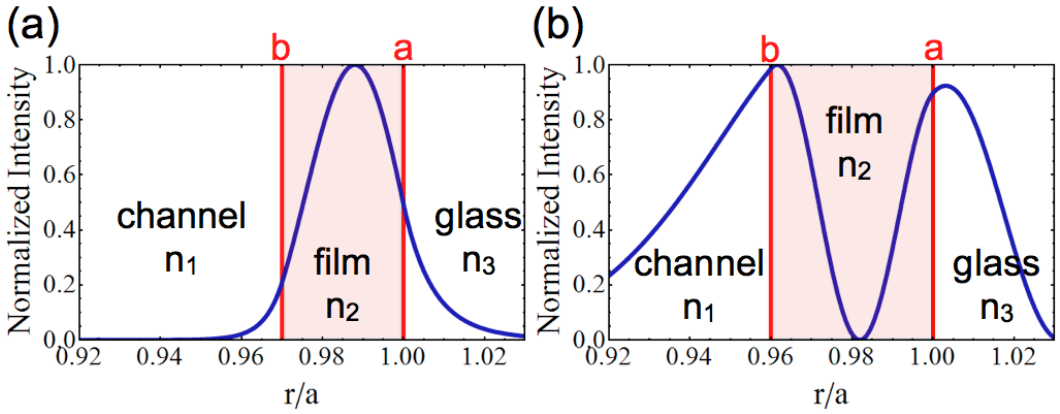

Figure 1.7 – Electric field profiles for a coated capillary (30 μm inner diameter). Here $n_1 = 1.33$, $n_2 = 1.675$ and $n_3 = 1.452$. The tail of the WGM field profile extends into the channel. Field profiles are given for (a) A first order radial mode with angular number $l = 190$, film thickness 450 nm and a resonant wavelength of 779 nm, and for (b) A second order radial mode with angular number $l = 90$, film thickness 600 nm and a resonant wavelength of 1305 nm.

There are two figures of merit that describe the sensing capabilities of WGMs in resonators. The first is the refractometric sensitivity:

$$S = \frac{d\lambda}{dn}. \tag{1.31}$$

Here, $d\lambda/dn$ is simply the "rate" at which the resonant wavelength changes as a function of the refractive index of the analyte. The sensitivity is an inherent property of the structure, *i.e.*, it is not related to the measurement system. The second figure of merit is the detection limit (DL), which is the minimum detectable refractive index change:

$$DL = \Delta n_{\min} = \frac{\Delta\lambda_{\min}}{S}. \tag{1.32}$$

The DL is dependent on the wavelength "resolution" of the measurement system,

$\Delta\lambda_{\text{min}}$. A small DL implies good device performance: ideally one has a large sensitivity and a small (*i.e.*, high) system resolution. The sensitivity and DL are the main figures of merit used in comparing different microresonator devices and quantifying their functionality as a biosensor.

1.4.1 Review of previous studies

A brief discussion of WGM-based refractometric sensing is useful as a standard for comparison. There are many different microresonator geometries that have been used for refractometric sensing including spheres [49–51], fibres [52], micro-ring/waveguides [53], capillaries [34, 54–56], and toroids [57]. For the most part, in these geometries the WGMs are excited by evanescent coupling to the resonator using a tapered fiber or a waveguide (Figure 1.8).

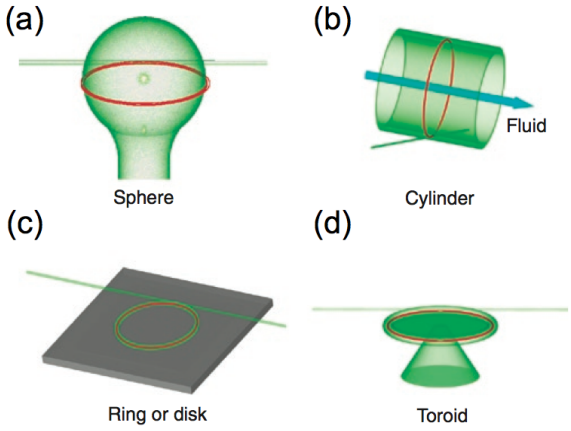

Figure 1.8 – Examples of whispering gallery mode resonators for a variety of structures including (a) Spheres, (b) Thin-walled capillaries, (c) Rings or disks, and (d) Toroids. Modified from Ref. [32].

However, some geometries are not entirely practical. For example, in microspheres, WGMs develop at the boundary between the sphere and the external environment (Figure 1.9(a)). For refractometric sensing, the microsphere therefore requires an external chamber, which is not the ideal situation for a microfluidic biosensing device. Additionally, evanescent coupling into the resonators can be difficult and finicky, requiring nanometer-precision positioning of the various elements.

1.4.1.1 Liquid Core Optical Ring Resonator

A new type of WGM-based sensor device was developed by a group at the University of Missouri-Columbia in 2006. This device is called a "liquid-core optical ring resonator" (LCORR) [47, 48]. A LCORR is a thin-walled glass microcapillary. In a LCORR, light is confined by TIR at the boundary between a thinned glass capillary wall and the outside air (Figure 1.9(b)). Analytes are pumped into the capillary channel, thus the field must extend into this region for sensing applications. This requires the capillary walls to be thin enough that the tail of the field profile can extend into the channel ($\sim 1\,\mu m$ thick).

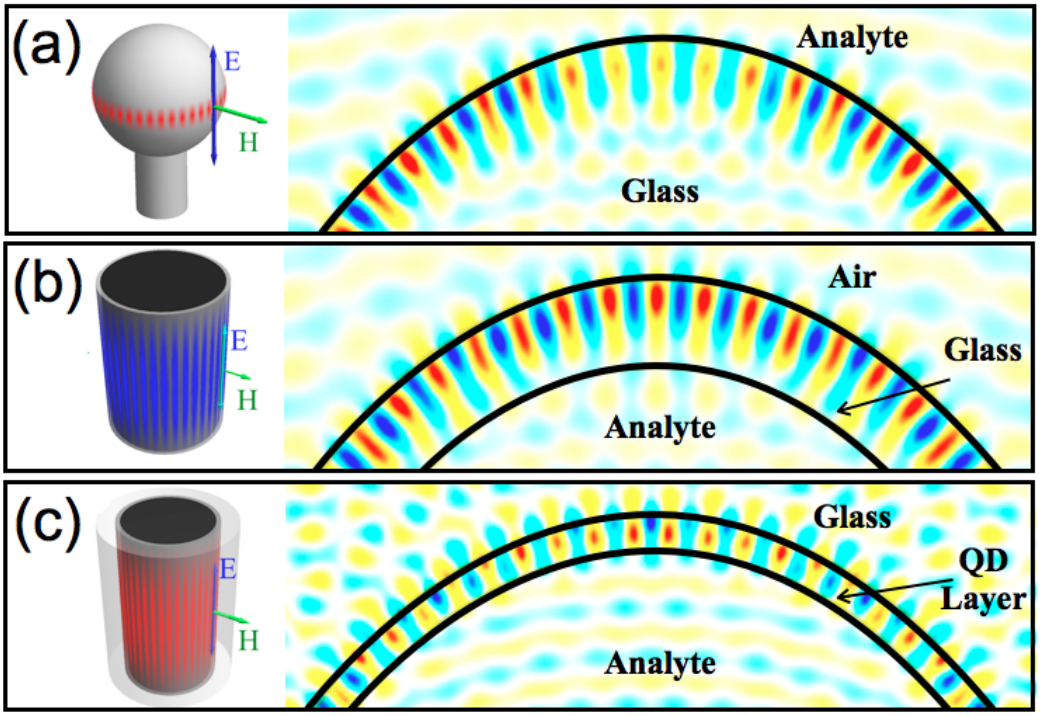

Figure 1.9 – Electric field amplitude for TE polarized WGMs of (a) A microsphere (b) A LCORR and (c) A FCM. The analyte is on the outside of the structure in the case of microspheres, and on the inside channel for LCORRs and FCMs. The radial mode order is equal to 1, while the angular orders are 53, 52, and 65, respectively.

LCORRs can be fabricated using two different methods. First, White *et al.* have developed a two step fabrication procedure. Fused silica glass capillaries are pulled while being heated by a torch or CO_2 laser to thin the outer walls of the capillary. Next, hydrofluoric acid (HF) is passed through the capillary to further thin the cap-

illary walls. The concentration of the HF solution and the etching time control the wall thickness. Using this method, LCORRs with an outer diameter > 100 μm were fabricated with walls $\lesssim 3$ μm thick. In a second method [34,58], Zamora *et al.* pressurized the capillaries by pumping an inert gas through them while the capillaries were heated and pulled simultaneously. This method also results in capillaries that have micron-scale wall thicknesses.

The LCORR has a variety of attractive properties (particularly over non-microfluidic geometries) but still has some limitations. The device has moderate to high Q factors ranging from $10^6 - 10^7$, sensitivities up to 390 nm/RIU for third-order radial modes [34], and detection limits near 10^{-6} RIU. [31,34,47,48,54,59,60]. They can be surface functionalized for analyte-specific biosensing applications [54, 59–63]. However, coupling light evanescently into the LCORR requires nano-positioning equipment and careful placement of a tapered waveguide (where the waveguide needs to be placed less than 1 μm away from the LCORR, as suggested in Sect. 1.3.1 where the evanescent field distance was estimated to be a few hundred nanometers). This requires extra care, since the required thin walls make the LCORR delicate and hard to handle. Another factor is that LCORRs require a precision tunable laser system (an expense upward of $20,000).

1.4.2 Fluorescent Core Microcapillaries

Fluorescent-core microcapillaries (FCMs) address some of the issues associated with LCORRs. The FCM, developed in our group, is a thick walled microcapillary in which the channel is coated with a fluorescent high-index QD film. Here, the WGMs will develop in the film, which, if sufficiently thin, permits the field to extend into the microfluidic channel (Figure 1.9(c)). This reduces the need for thinning the capillary walls, making the device more durable. A high-index coating has been applied to other microcavity structures such as microspheres [51,64,65] and fibres [52], however it has not previously been used to create a fluorescent WGM-supporting layer in a microcapillary.

The advantages of these devices over LCORRs are that (i) the FCM is mechan-

ically robust and (ii) excitation of fluorescence WGMs requires an inexpensive laser diode or LED rather than a tunable laser system. Thus, there is no need for nano-positioning systems. The fluorescence can be collected and analyzed using standard spectroscopic techniques, which eliminates the need for expensive tunable lasers required by LCORRs. The FCM demonstrates moderate Q-factors from 10^2–10^3, a DL approaching 10^{-4} RIU and sensitivities from 7–20 nm/RIU [55,66]. Thus, FCMs have a specific set of advantages and limitations with respect to LCORRs. This device (Figure 1.10) was first presented in the Master's work of Kyle Manchee in 2011 and was the first of its kind to demonstrate refractometric sensing.

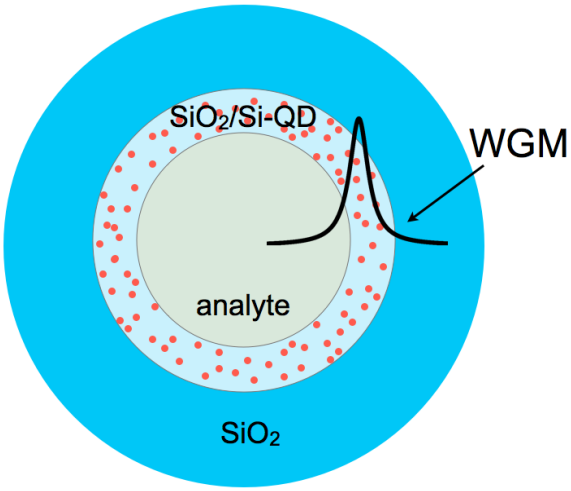

Figure 1.10 – Structure of the FCM. The film consists of Si-QD in an SiO_2 matrix.

1.5 Silicon quantum dots

The FCM to be investigated in this work has a high-index layer consisting of fluorescent silicon quantum dots (Si-QDs) embedded in a SiO_2 matrix (Figure 1.10). The Si-QDs are typically 3-8 nm in diameter, showing atomic lattice planes and diffraction patterns characteristic of crystalline silicon (Figure 1.11). Silicon is preferred for sensor applications because of its low toxicity and photochemical stability [67, 68]. Importantly for this work, our group developed a specialized coating method for Si-QDs that can be readily extended to capillaries [55,69] (a process that will be described in Chapter 2). One of the most important properties is that the surface of the

QD layer is essentially composed of silica. The surface chemistry, being silica-based, should thus be amenable to functionalization with existing recipes [49,56,61,62,70]. The purpose of this section is to describe the nature of the silica-based Si-QD film and the light-emission process.

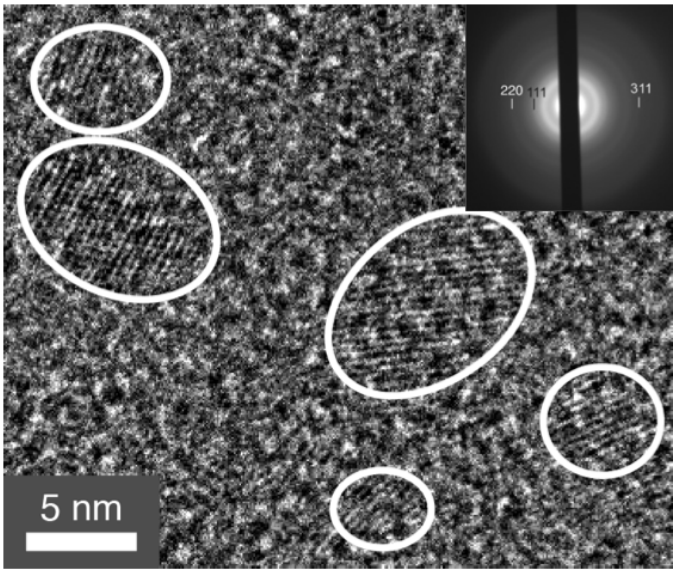

Figure 1.11 – High resolution TEM micrograph of a flat Si-QD film, showing randomly-oriented Si-QDs with radii from 2-4 nm. Inset shows selected-area electron-diffration pattern where the rings are representative of Si [71,72].

Bulk silicon (Si) is a poor optical emitter due to its indirect band gap, which is at an energy of 1.12 eV [67,73]. This causes a small radiative recombination rate for excited electrons and holes, owing to the second-order processes that require the emission of both a phonon and a photon to conserve energy and momentum [74]. Compared to direct gap materials, the radiative lifetimes are much longer, thus increasing probability for non-radiative decay processes to occur.

The luminescence efficiency (or quantum efficiency), η_R, can be given by

$$\eta_R = \frac{1}{1 + \tau_R/\tau_{NR}}, \tag{1.33}$$

in which τ_R and τ_{NR} represent the radiative and non-radiative lifetimes, respectively [74]. Efficient luminescent systems (*i.e.*, large η_R) will be ones in which the radiative lifetime is much shorter than the non-radiative lifetime ($\tau_R \ll \tau_{NR}$). For indirect

bandgap materials such as silicon, in which there is competition with non-radiative recombination, *i.e.*, $\tau_R > \tau_{NR}$, the quantum efficiency can be small. [74].

A way to improve the fluorescence efficiency in Si is by controlling the QD size and shape [74–77]. For silicon quantum dots in the strong quantum confinement regime, the smallest transition across the bandgap for the first excited level can be approximated by

$$E = E_g + \frac{\hbar^2 \pi^2}{2\mu R_0^2} - 1.786 \frac{e^2}{\varepsilon_r \varepsilon_0 R_0}, \tag{1.34}$$

where μ is the electron-hole reduced mass ($\mu^{-1} = m_e^{-1} + m_h^{-1}$), e is the electron charge (1.6022×10^{-19} C), ε_0 is the electric permittivity of free space, ε_r is the relative permittivity, and R_0 is the radius of the QD. Quantum size effects cause continuous energy spectrum in the conduction and valence bands of bulk Si to become discrete [74, 78, 79] (Figure 1.12). The confinements shifts the band gap of bulk Si from 1.12 eV to around 3 eV for a particle 2 nm in diameter [80].

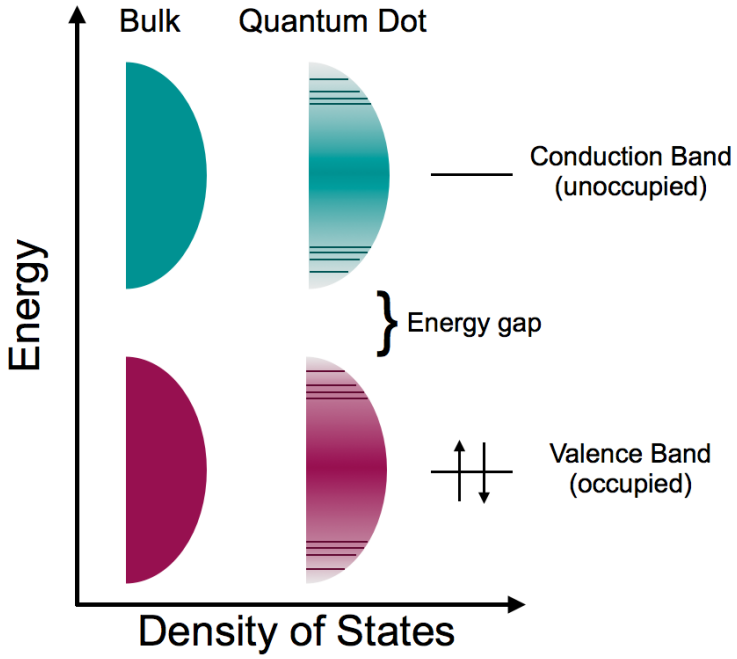

Figure 1.12 – Schematic of the density of states for bulk materials and quantum dots. As the dimension of the particle decreases, the DOS forms continuous energy bands. Modified from [78].

Electronic grade bulk Si has quantum efficiencies typically in the range of 10^{-6}

[81]. In Si-QDs the efficiency can increase by 4 to 6 orders of magnitude [82] and there have been reports of quantum efficiencies as high as 0.6 for Si-QDs [83, 84]. The increased efficiency is in part a result of the physical confinement which restricts carrier migration to non-radiative traps [68, 74, 75, 79]. The photoluminescence (PL) of the Si-QDs used in this work has a central emission wavelength near 800 nm (Figure 1.13), whose origin has been attributed both to "pure" quantum confinement [75] and to sub-gap emissive centres [85].

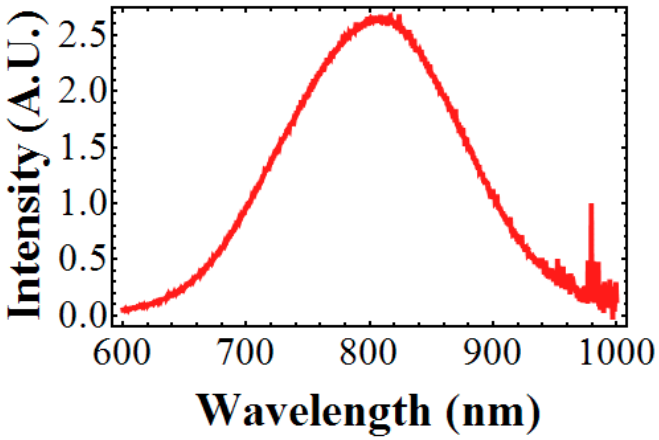

Figure 1.13 – Photoluminescence of a Si-QD flat film, fabricated from annealing solid HSQ.

1.5.1 SiO_2 functionalization for biotin and streptavidin

Here the mechanism for the chemistry will be described. It is important to understand these reaction mechanisms as they will aid in the explanation of the results to be described in Chapter 4.

In this work, we are interested in the demonstration of biosensing on the silica channel of the FCM. Biotin and streptavidin are commonly used as a proof-of-principle system for biosensing applications because of their strong affinity and relatively well-understood binding chemistry [49, 60, 86, 87]. Biotin binds to streptavidin with high specificity and affinity (biotin and streptavidin have a dissociation constant $K_d \approx 4 \times 10^{-14}$ mol/L). Biotin and streptavidin form a stable system that is resistant to extremes of heat, pH, and solvent [88–90].

Biotin (also known as vitamin H) is a small, water-soluble molecule that has a molar mass of 0.24431 kg/mol [88]. Biotin may be difficult to detect in optical systems; thus biotinylated Bovine Serum Albumin (BSA-biotin) was used in this work. BSA-biotin has a molecular weight of 66.43 kg/mol [38]. Streptavidin[7] (SA) is a tetrameric protein and has a molar mass of 59.999 kg/mol [91].

The binding mechanism for biotin and streptavidin is one of the strongest non-covalent interactions known [91]. The bond itself has three binding features: hydrophobic and van der Waals forces, hydrogen bonds and a binding surface loop in streptavidin which folds over biotin [91]. Up to four biotin molecules can bind to a single streptavidin molecule.

SiO_2 surfaces are hydroxyl terminated, preventing the binding of biotin to the capillary wall. However, biotin can attach to a surface that is terminated with an amine (-NH_3) end group. Amine termination can be achieved through the silanization of the SiO_2 surfaces. The silanization is performed with alkoxysilane groups such as methoxy (-OCH_3) and ethoxy (-OCH_2CH_3) in the form of aminosilanes: (3-aminopropyl)-triethoxysilane (APTES) and (3-aminopropyl)-trimethoxysilane (APTMS), respectively [94].

The mechanism of functionalizing the surface with the aminosilane is a two step reaction. The first step involves the removal of the alkoxy groups from the alkoxysilane molecule via hydrolysis (breaking of chemical bonds by water) (Figure 1.14(a)). This reaction is self-catalyzed by the amine group [95], however the presence of water acts as a catalyst to increase the rate of reaction [93]. This results in the formation of hydroxylsilane and either methanol or ethanol (depending on whether APTES or APTMS was used). In the second step, the hydroxylsilane covalently binds to the -OH terminated silicon surface by the removal of an H_2O molecule and the formation of a -Si-O-Si- bond [96]. This is the "condensation" step, which results in an NH_3-terminated (3-aminopropyl)-siloxane (APS) film on the surface (Figure 1.14(b)).

One complication is that the creation of the functionalization layer is sensitive to the reaction conditions, *i.e.*, solvent, temperature, amount of water, reaction tem-

[7]Purified from the bacterium *Streptomyces avidinii*.

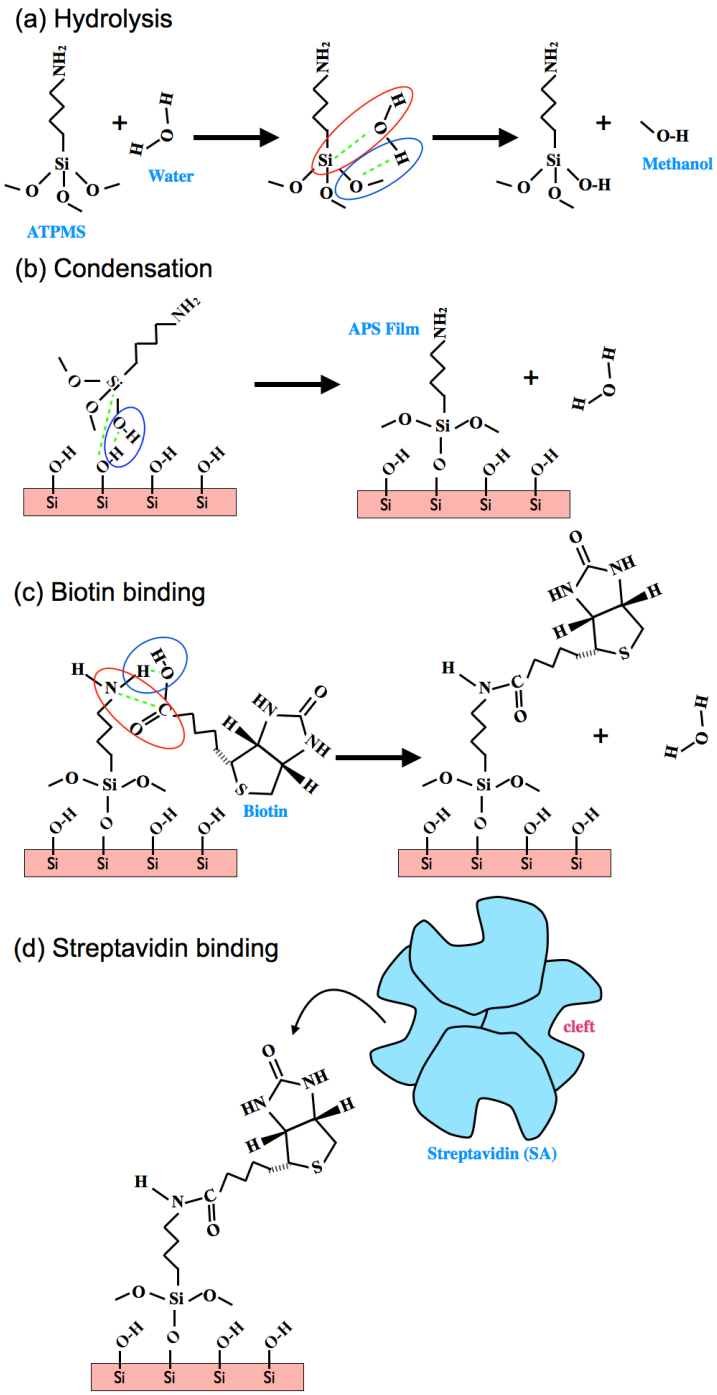

Figure 1.14 – Schematic showing how the surface is functionalized by APTMS. (a) Hydrolysis reaction in which a water molecule breaks the alkoxy bond of the APTMS molecule, forming hydroxylsilane and methanol (b) Condensation reaction where the Si from the intermediate group binds to the oxygen atom on the silicon dioxide surface producing an APS layer, releasing a water molecule. This reaction is sensitive to the water concentration in the solution. (c) Biotin binding to the amino-end group by the formation of an amide bond, along with the release of another water molecule. (d) Finally a cleft from streptavidin will bind to the biotin group. Modified from Ref. [92] and [93].

perature and concentration of silane [93, 97]. These factors can affect the thickness of the silane layer, its surface roughness, and the geometrical bonding arrangement on the surface [98].

Once the Si-QD surface has been functionalized, the specific attachment of biomolecules should be possible. If in the proper orientation, the amine group allows for the attachment of the proteins. Biotin can be attached via a covalent amine-termination forming an amide bond (Figure 1.14(c)) [92]. Streptavidin can then be subsequently attached via the SA cleft and any other biotinylated biomolecules can then be attached to SA at other cleft points (Figure 1.14(d)).

1.6 Project objectives

First, for any biosensing device, it is necessary to know the capabilities of the sensor, *i.e.*, the detections limits and sensitivity. This will determine whether, indeed, a detection will be possible for a given analyte. Biosensing has never been done with FCMs; thus, the first objective was to determine the sensitivity (S) and detection limits (DL) of the device. Essentially, the first question is "can we do biosensing with these structures at all"?

The second aspect of the project is to demonstrate the "live-time" sensorgram capabilities of the FCM. More information can be gathered by use of a sensorgram, rather than via static measurements. Up until this work, only static measurements have been done with FCM devices.

The third objective was to test and evaluate the feasibility of the FCM as a biosensor. While FCMs have been demonstrated for refractometric sensing [55, 71], this work was the first attempt at biosensing with these devices. The biotin-streptavidin system was selected as a standard biological test system for this reason.

Chapter 2

Experimental methods

2.1 Fabricating the FCM

2.1.1 Capillary preparation

Fabrication of the FCM starts with commercially available fused-silica tubing capillary, purchased from Polymicro Technologies [99]. The capillaries have a 25 or 30 μm inner diameter (ID) and a 363 μm outer diameter (OD). The capillaries come from the manufacturer in spools and are coated with a 20 μm protective flexible polyimide cladding (Figure 2.1).

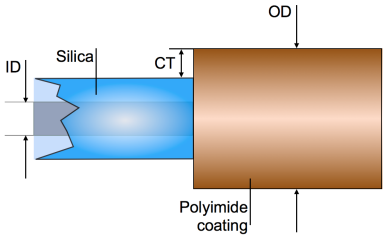

Figure 2.1 – Diagram of the capillary tubing. Modified from Ref. [99].

The purchased capillaries are cleaved into approximately 10 cm pieces (about 10–20 of them per batch) by scoring the surface with a diamond scribe and snapping them off the spool. This method is used to prevent the inner walls from pinching off and closing the channel (which can be a problem when using optical fibre cleavers). The length of the cleaved capillaries is determined by the available space on the

microscope stage.

All capillaries were placed into a glass boat that was cleaned using pentane or isopropyl alcohol (IPA). The boat was transferred to a Barnstead Thermolyne 21100 tube furnace. The tube was evacuated with a roughing pump and backfilled with oxygen. The capillaries were then annealed at 650°C for 45 minutes under a steady flow of O_2. This process ashes the polyimide cladding and exposes the silica capillary. After the ashing procedure, the capillaries were removed and stored in a petri dish until they were ready to be used.

2.1.2 Creating the Si-QD layer

Hydrogen silsesquioxane (HSQ) was used as the precursor agent to create the oxide embedded Si-QDs on the inner channel of the capillary. The HSQ molecule has the chemical formula $H_{12}Si_8O_{12}$ and is available commercially in a solution form called flowable oxide (FOx). FOx consists of solid HSQ dissolved in methyl isobutyl ketone (MIBK)[1], and is available from Dow Corning [100]. The FOx solutions come in a variety of different concentrations of HSQ by weight (w/w); for example FOx-15 (used here) is nominally 18% w/w HSQ.

The capillaries were dipped into the HSQ precursor solution and the fluid was drawn up the channel via capillary forces. Previous work has shown that the ultimate film structure (thickness and uniformity) is sensitive to the HSQ concentration and is dependent on capillary diameter [69, 71]. Here, capillaries with 25–30 μm ID were used, which according to previous work, requires ∼20–25% w/w HSQ to create good Si-QD films on the channel surface.

The annealing temperatures and time controls the size (and therefor the luminescence) of the QDs [101]. In previous work [71], a two-step annealing process was used. According to this procedure, the first annealing step is a dwell at 300°C for 2–3 hours. This step evaporates the solvent and adheres the HSQ to the capillary walls. In the second step, the capillaries are heated to at 1100°C and held at this temperature for $\sim$ 1 hour. This causes the crystallization and growth of Si nanodomains in a

[1] FOx solutions also contain very minute concentrations of Toluene (1–5% w/w).

silica-like matrix. The capillaries are then slowly cooled to room temperature, over a 12-hour time period. This helps to reduce stress cracking, resulting in a uniform film inside the capillaries.

From multiple fabrication attempts, success or failure seems to hinge on small differences from run to run (*e.g.* the age of the solution, the environmental conditions and how the chemicals are stored). Small amounts of humidity from the atmosphere can cause rapid gelation, making it impossible to draw the solution into the capillaries. Therefore, all solutions were mixed (and all chemicals are stored) in an argon glove-box. Nevertheless, the success rate was found to vary considerably in different runs.

2.1.3 Hydrogen silsesquioxane precursor solution

Several different methods were employed to create the HSQ precursor solutions that were used to produce the Si-QD film on the inner channel of the capillaries. The process was modified throughout the experimental process. Several different methods can be employed to make the precursor solution:

1. Dilute the FOx solutions using a solvent (m-xylene or MIBK)[2]
2. Increase the FOx solution by adding solid HSQ
3. Fabricate "home-made" solutions using solid HSQ and a solvent (m-xylene or MIBK)

Solid HSQ in the form of a white powder was obtained from Dow Corning. This product is no longer commercially available, so solid HSQ can also be produced by evaporating the solvent from FOx solutions, using a vacuum gas manifold (Schlenk line). Here, a few milliliters of FOx solution can be placed on the Schlenk line and the solvent can be vaporized overnight, leaving behind solid HSQ. The precursor solutions in this thesis were mixed using steps 2 or 3, where the solid HSQ was the commercially available powder from Dow Corning.

[2]Used during fabrication of the Si-QD film in larger diameter capillaries (>40 μm).

Increasing the concentration of FOx-15 solution As been previously determined, the concentration needed to produce Si-QD films is ∼20–25% w/w HSQ for a 25 or 30 μm inner diameter (ID) capillary [71]. Some very simple calculations can be used to quickly estimate the masses needed. The mass of the FOx solution will be denoted as m_{FOX} and the mass of the HSQ in the FOx solution to be m_{HSQ}. The FOx-15 solution used is 18% w/w HSQ, meaning

$$m_{HSQ} = 0.18 m_{FOX}. \tag{2.1}$$

The mass of solid HSQ added to the mixture will be denoted as m_{add} and thus the total HSQ in the solution will be

$$w_{HSQ} = m_{add} + m_{HSQ} = m_{add} + 0.18 m_{FOX}. \tag{2.2}$$

The concentration of the solution, C, mixed (by weight) in terms of the quantities that can be directly measured:

$$C = \frac{w_{HSQ}}{w_{total}} = \frac{m_{add} + 0.18 m_{FOX}}{m_{add} + m_{FOX}}. \tag{2.3}$$

The value of C for 25–30 μm diameter capillaries has been previously determined to be between 0.2–0.25 [71]. However, because the FOx solutions degrade over time, the value of C changes as well, requiring some trial and error.

The easiest way to create the solution is to first weigh out the solid HSQ and then weigh out and add the FOx-15 needed to get the desired final concentration. For example, if aiming for a 25% HSQ w/w solution:

$$C = 0.25 = \frac{m_{add} + 0.18 m_{FOX}}{m_{add} + m_{FOX}}, \tag{2.4}$$

$$(0.25)(m_{add} + m_{FOX}) = m_{add} + 0.18 m_{FOX}, \tag{2.5}$$

which rearranging gives

$$m_{FOX} = \frac{0.75}{0.07} m_{add} \approx 10 m_{add}. \tag{2.6}$$

Thus, the solution requires approximately ten times more FOx-15 solution by weight than solid HSQ.

"Home-made" solutions using solid HSQ and a solvent In this work, most of the time the solution was made "from scratch". This was done by adding solid HSQ to a solvent, either m-xylene (m_X) or MIBK (m_M). Again, the concentration was determined by weight, albeit using a much simpler calculation, and mixed for the desired concentration based on capillary size (C = 0.2–0.25 for 25–30 μm ID capillaries):

$$C = \frac{w_{HSQ}}{w_{total}} = \frac{m_{add}}{m_X}. \tag{2.7}$$

2.1.4 Capillary filling and annealing

After the solutions were mixed, the next step was to fill the capillaries with the solution. Small vials containing the prepared precursor solutions were removed from the inert environment. One end of each capillary was dipped into each solution and the fluid was drawn up via capillary forces (Figure 2.2(a)). The capillary was held until the meniscus reached the top of the capillary. This procedure took ∼15–30 seconds per capillary. Typically, 10 capillaries were filled with each of the two precursor solutions. The capillaries were then placed in cleaned glass crucibles. The boats were transferred to a Lindberg/Blue M tube furnace.

The annealing procedure was as follows:

1. Ramp up to 300–350°C at a rate of 10°C/minute.
2. Dwell at 300–350°C for 3 hours (300°C for FOx solutions, 350°C for "home-made" solutions).
3. Ramp up to 1100°C at a rate of 17°C/minute.

4. Dwell at 1100°C for 1 hour.

5. Cool to room temperature over approximately 12 hours.

The capillaries were annealed (and cooled) under a flow of either 5% H_2 + 95% Ar or 5% H_2 + 95% N_2.

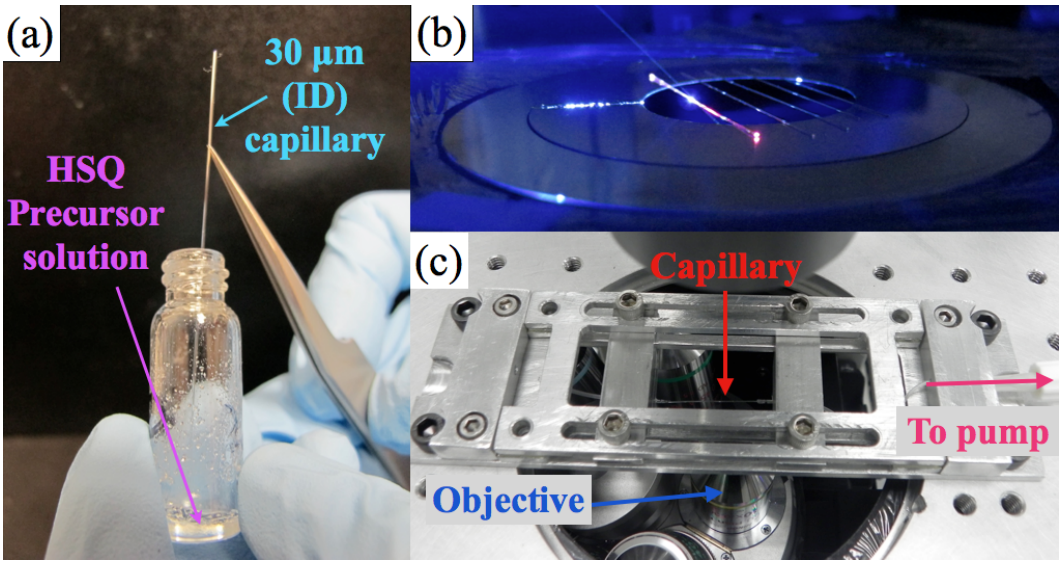

Figure 2.2 – (a) Filling the capillary with HSQ precursor solution via capillary forces (b) Checking annealed capillary samples for PL and WGMs (c) Capillary interfaced to a microsyringe pump.

2.2 Sample characterization

2.2.1 Fluorescence imaging and spectroscopy

The capillaries were mounted on the stage of a Nikon Eclipse TE 200-e inverted microscope interfaced to a Santa Barbara Instrument Group (SBIG) self guided spectrograph (SGS) with a ST-7XME CCD camera. The fluorescence was pumped in the free space on the microscope stage using several different sources (Figure 2.2(b)):

- the 488 nm line of an Ar^+ laser ($\sim$ 40 mW)
- 405 nm laser diode ($\sim$ 200 mW)
- 445 nm GaN laser diode ($\sim$ 150 mW)

The fluorescence was collected by the microscope objective, sent through an analyzer, and then through a long-pass filter to remove scattered laser light. The spectrograph has an 18 μm-wide entrance slit and a 600 lines/mm grating blazed at 750 nm. It has a manufacturer-quoted resolution of 0.24 nm and a pitch value of 0.104 nm/pixel. To help reduce detector noise, the CCD camera interfaced to the spectrometer was cooled to -15°C. The manufacturer-supplied computer software CCDOps was used to capture raw spectral images as 16-bit TIFF files.

Capillaries with WGMs in the fluorescence spectra were glued to polyethylene tubing (PE) [102] with an inner diameter of 0.015" using Mascot Instant Adhesive gel. The tubing was interfaced with a 1 mL Beckton-Dickson plastic syringe attached to Chemyx Nanojet syringe pump (Figure 2.2(c)). The fluids for all experiments were pumped at a constant rate of 0.002 mL/min.

Fluorescence measurements were obtained in both static and sensorgram format. For static measurements the solution was pumped into the capillary. The pumping was then stopped and an exposure was taken. For sensorgram analysis, 20-second spectral images were continuously collected while solutions were pumped through the capillary.

2.2.2 Calibration

The first step was to calibrate the wavelength dependence of the spectrometer efficiency. This was accomplished using an Ocean Optics HL-2000 FHSA Tungsten Halogen blackbody light source with a colour temperature of 3100 K. The calibration takes the simple mathematical form

$$S(\lambda) = s(\lambda)\frac{I_{\lambda,T}(\lambda)}{B_{\lambda,T}(\lambda)}, \tag{2.8}$$

where $S(\lambda)$ is the intensity-calibrated PL spectrum, $s(\lambda)$ is the raw PL spectrum (Figure 2.3(b)), $B_{\lambda,T}(\lambda)$ is the collected black body spectrum (Figure 2.3(c)), and $I_{\lambda,T}(\lambda)$ is the Planck spectrum at 3100 K. The second step in the calibration process was to convert the CCD pixel value into a wavelength. This was achieved using the

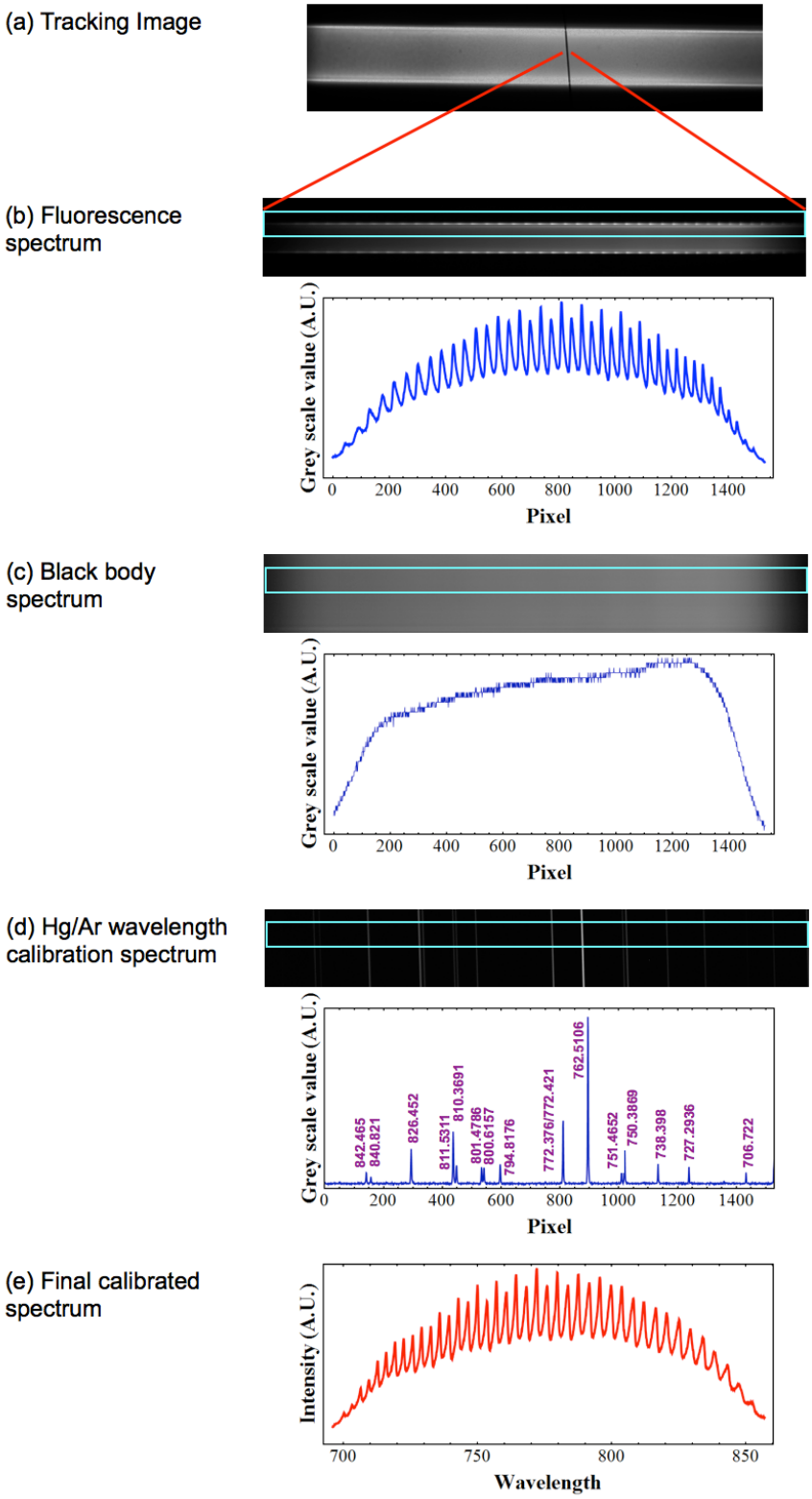

Figure 2.3 – Calibration of WGM spectra. (a) Fluorescence image of a capillary channel, showing the spectrometer entrance slit. (b) Fluorescence spectral image showing the uncalibrated WGM spectrum. (c) Blackbody spectral image and intensity profile. (d) Hg/Ar spectral image and intensity profile for wavelength calibration. (e) Final calibrated WGM spectrum.

known spectral lines of a Hg/Ar lamp (Figure 2.3(d)). The entire calibration process was automated using a *Mathematica* code.

2.3 Sensor characterization

2.3.1 Refractometric sensitivity

The refractometric sensitivity was determined using solutions of different concentrations of sucrose in water, or by sequentially pumping distilled water, methanol (CH_3OH) and ethanol (C_2H_5OH) through the capillary. Using sucrose solutions permitted small changes in the refractive index to be achieved relatively easily, which was helpful for investigating the analysis techniques to be described in Chapter 3. The second method (methanol, water, and ethanol) was quicker and ensured that the inner channel of the FCM remained clean, for subsequent biosensing experiments (Chapter 4).

The refractive index of the sucrose solutions was calculated using the formula

$$n = (0.14287)C_s + 1.333029, \tag{2.9}$$

where C_s is the concentration of the sucrose solution in units of g/L [103]. Eleven solutions were prepared with increasing sucrose concentration, as summarized in Table 2.1. The dispersion of these sucrose solutions is unknown, although (given the low sucrose concentrations) it is probably not too different from that of water. The refractive index was increased in steps of 0.0012 refractive index units (RIU).

The refractive indices of methanol, ethanol and distilled water are well known. All refractive indices were calculated at 800 nm, near the centre of the PL spectrum. For ethanol, the dispersion formula [104]

$$n = 1.35265 + 0.00306\lambda^{-2} + 0.00002\lambda^{-4}, \tag{2.10}$$

gives a refractive index of 1.35748. The dispersion relation for methanol is [105]

$$n = 1.294611 + 12706.403 \times 10^{-6}\lambda^{-2}, \tag{2.11}$$

which gives a refractive index of 1.31446 at 800 nm. The refractive index for distilled water is 1.32861, calculated from the dispersion formula [106]

$$n^2 - 1 = \frac{5.68 \times 10^{-1}\lambda^2}{\lambda^2 - 5.10 \times 10^{-3}} + \frac{1.73 \times 10^{-1}\lambda^2}{\lambda^2 - 1.82 \times 10^{-2}} + \frac{2.09 \times 10^{-2}\lambda^2}{\lambda^2 - 2.62 \times 10^{-2}} + \frac{1.13 \times 10^{-1}\lambda^2}{\lambda^2 - 1.07 \times 10^{1}}. \tag{2.12}$$

Table 2.1 – Sucrose concentration and refractive index

Solution Number	Sucrose Concentration (g/L)	Refractive Index	Notes
0	0	1.333	Pure distilled water
1	8.0	1.3342	
2	16.0	1.3353	
3	24.0	1.3365	
4	32.0	1.3376	
5	40.0	1.3387	
6	48.0	1.3399	
7	56.0	1.341	
8	64.0	1.3422	
9	72.0	1.3433	
10	80.0	1.34446	"stock solution"

2.3.2 Biosensing Measurements

To test the FCM in a biosensing application, a protein binding system of biotin-streptavidin (or avidin) was used. Both BSA-biotin and streptavidin come as white filamentary solids, obtained from Vector Laboratories Canada [107, 108]. They are reconstituted with distilled water and stored at 4 °C.

The recipe for the biotin/streptavidin experiment was modified from Refs. [49] and [109]. The first step was to functionalize the QD-layer with an amine linker. The experiment was conducted by pumping solutions through the capillary in the following order:

1. 90%/10% methanol/deionized water solution.
2. 2% (3-aminopropyl)-trimethoxysilane (APTMS) in 90%/10% methanol/deionized water solution.
3. 90%/10% methanol/deionized water solution.
4. 100% methanol.
5. 100% deionized water.
6. 10 nM of phosphate buffer saline (PBS)[3] in deionized water.
7. 0.1 mg/mL solution of BSA-biotin in 10 nM PBS.
8. 10 nM PBS.
9. 20 μg/mL solution of streptavidin in 10 nM PBS.
10. 10 nM PBS.

Two blank runs were also performed. In the first run, the procedure just described was followed but without the initial functionalization (steps 1 and 2). In the second blank run, the full procedure was performed (steps 1-10); however step 9 instead consisted of a pre-mixed solution of BSA-biotin and streptavidin in 10 nM PBS (with concentrations of 0.1 mg/mL and 20 μg/mL, respectively).

Fluorescence spectra were collected while these solutions were pumped at a rate of 0.002 mL/min through the capillary. Spectra were taken in 20-second intervals in order to measure the WGM shifts as each solution was pumped through the channel. This produced a "time series" of spectral images for subsequent processing.

[3]PBS has a pH of 7.4.

Chapter 3

WGM shift analysis: sensitivity and detection limits

3.1 Initial sample evaluation

The first step was to determine whether the FCM fabrication was successful. The capillaries were placed on the microscope and excited with a blue laser diode to excite the fluorescence. Those samples that were deemed "successful" exhibited WGMs in the fluorescence spectra.

Taking spectra from each capillary can be time consuming. Therefore, some basic visual trademarks were employed for quick analysis of each capillary. First, some samples contained no visible fluorescence (Figure 3.1(a)). This is likely due to a capillary being clogged during the filling step of the sample preparation. Secondly, some samples exhibited orange fluorescence that routinely did not show WGM oscillations in the spectra (Figure 3.1(b)). As can be seen in the figure, the orange fluorescence was concentrated in the middle of the channel and does not seem to originate from the edges. The remaining samples showed a red fluorescence. Some of the capillaries with red fluorescence showed WGMs in the spectra (Figure 3.1(d)). However, as shown in Figure 3.1(c), some red-emitting samples did not show WGMs in their fluorescence spectra. Generally the success rate varied from ∼20% in "good"

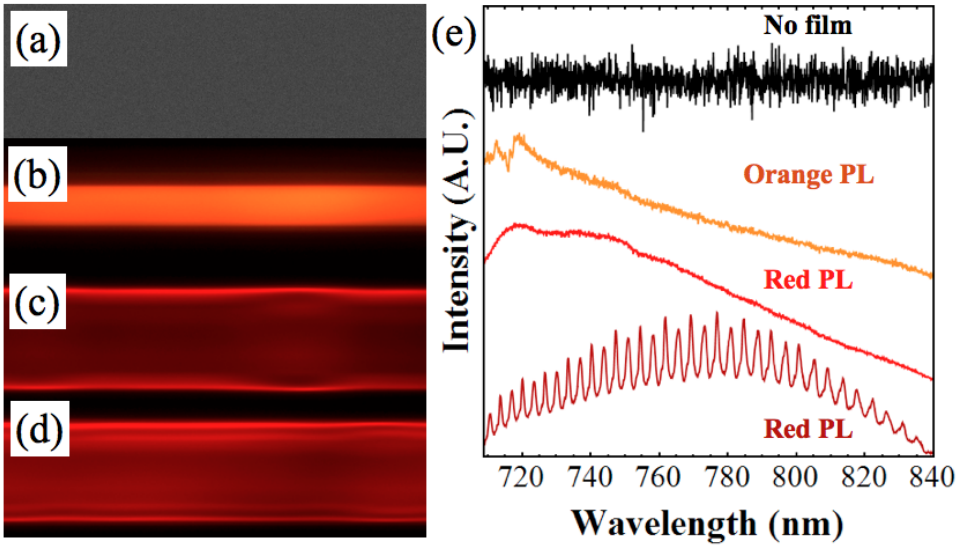

Figure 3.1 – PL images for the corresponding film type: (a) No film (b) Orange fluorescence (c) Red fluorescence with no modes (d) Red fluorescence with modes present. Spectra (c) and (d) were taken on different parts of the same sample showing non-uniformity throughout the length of the capillary. The calibrated spectra in (e) correspond their particular fluorescence images in order from top to bottom (a-d).

batches, to complete failure (no successes) in repeated runs.

Figure 3.2 demonstrates a successful sample where there is a region of good-quality QD film, without any visible cracks or delamination in both transmission and fluorescence images. Transmission images of the capillary revealed the QD film as a brownish-yellow colour. The fluorescence was reddish in colour and was brightest near the edges of the capillary channel. An end-on view of such a capillary revealed a ring-like band of fluorescence close to the edge of the channel, defining the QD film.

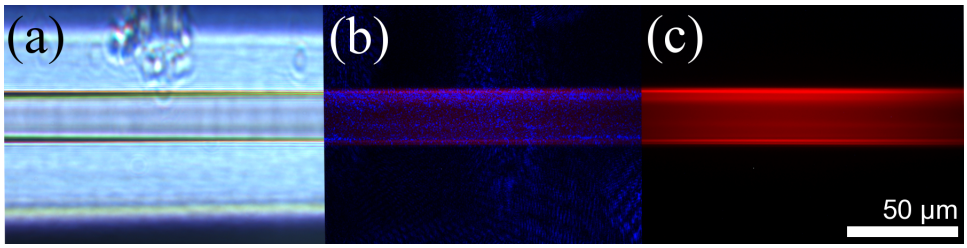

Figure 3.2 – Capillary images: (a) Transmission image, (b) Fluorescence using 405nm excitation source, (c) Fluorescence image with laser light filtered out.

Previous work determined the thickness of the Si-QD film inside the capillaries

using scanning electron microscopy (SEM) on both flat films and in capillaries [55,71]. The thickness was anywhere between 0.5 to 1 μm, and the film appeared smooth over the length of capillary imaged [55, 71]. The refractive index for the Si-QD film was determined on a flat, spin-coated film using variable angle spectroscopic ellipsometry (VASE) and found to be 1.672 at a wavelength of 800 nm [71].

3.2 Mode characterization and polarization

A linear polarizer was used to discern TE and TM polarized WGMs. The TE modes have the electric field parallel and the magnetic field perpendicular to the FCM axis; the opposite is true for TM polarization. As demonstrated in Figure 3.3, TE modes have a higher visibility than the TM polarized WGMs. The TE modes are characterized by Q-factors of about 700, whereas TM modes have Q-factors around 400. Both polarizations have a free spectral range (FSR) of approximately 4-5 nm and a finesse of $\sim$2. Because of their greater visibility and Q-factor, sensing experiments were performed using TE modes only.

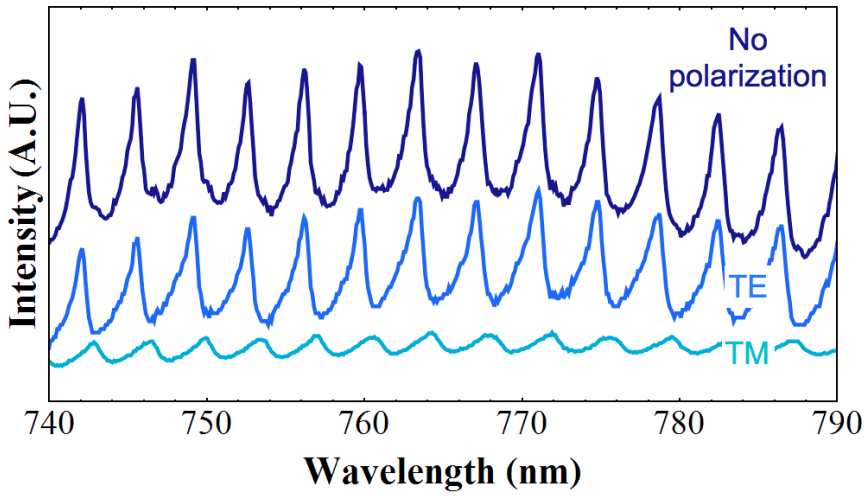

Figure 3.3 – WGM spectra in the absence of an analyzer (no polarization) and with the analyzer positioned to transmit either TE or TM polarized WGMs.

3.3 Experimental WGM spectral shifts

In order to find the optimal methods to determine the WGM wavelength shifts, two experiments were performed. First, WGM spectra were obtained over a narrow range of refractive index using sucrose-in-water solutions. Since it is easy to weigh and mix small quantities of sucrose, a narrow range of solution refractive indices, with arbitrarily small steps could be used. For these experiments, the step size was 0.0012 RIU. Each solution was pumped through the channel and spectra were taken using a 4-minute exposure to ensure good sampling and signal-to-noise ratio (SNR) (Figure 3.4(a) and (b)). The WGM wavelength shift for each refractive index step can be determined using various methods, which will be discussed in the following section.

A second set of measurements were collected over the same refractive index range (1.333–1.344), in which the exposure times were varied (Figure 3.4(c)). Reducing the exposure time decreases the SNR but, obviously, makes the measurements faster. This can be useful for many applications. Here, collection times of 4 minutes, 10 seconds, 1 second and 0.1 seconds correspond to SNR values of 300,000, 1000, 6 and 0.5, respectively.

There are at least two key features evident in these results (Figure 3.4) that will be important when determining the best method for quantifying the WGM wavelength shifts. First, the peaks are skewed towards shorter wavelengths. As will be shown, this lead to issues for finding the WGM shifts by curve fitting methods. Second, the spectral sampling is fairly poor (*i.e.*, there are typically only 30–40 data points defining individual WGMs). This is a consequence of the 0.104 nm/pixel pitch of the spectrometer used in these experiments.

3.4 Quantifying WGM spectral shifts

The WGM peak wavelength shifts in response to a change in the refractive index of the fluid in the capillary. Therefore, accurate measurement of the WGM spectral shift is important, as this will ultimately determine the detection limit of the

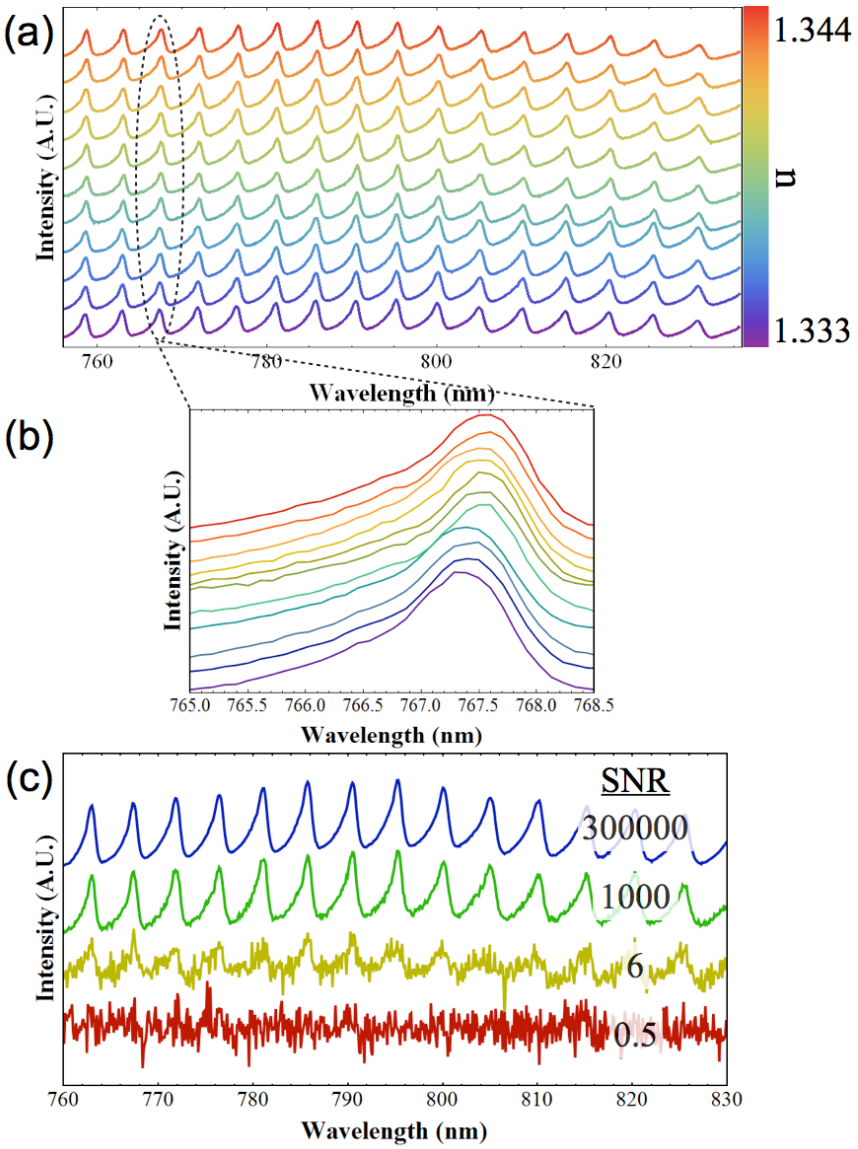

Figure 3.4 – (a) WGM spectra for increasing refractive index in 0.0012RIU steps in a 25 μm diameter capillary. (b) A "zoom-in" of a single peak from the WGM spectrum in (a). The wavelength shift is less than 0.25 nm. (c) Spectra collected over four different exposure times: 240 s, 10 s, 1 s, and 0.1 s, with the corresponding SNR. These spectra were taken with water inside the capillary.

structure. In this work, three methods were studied to measure the shift: (i) peak picking (PP), *i.e.*, the maximum value of a single WGM, (ii) curve fitting (CF) of individual WGMs, and (iii) Fourier transform (FT) analysis of the whole spectrum.

First, the spectra were transformed from intensity as a function of wavelength, $S(\lambda)$, into intensity as a function of frequency, $S(f)$ via:

$$f = \frac{c}{\lambda}, \tag{3.1}$$

$$S(f)\mathrm{d}f = S(\lambda)\mathrm{d}\lambda \tag{3.2}$$

$$S(f) = S(\lambda)\frac{c}{f^2}. \tag{3.3}$$

This transformation was performed after the calibration and black body corrections. Since the free spectral range (FSR) is constant in frequency units, this conversion makes the WGM spectral mode spacing periodic.

3.4.1 Curve Fitting

In order to find the peak wavelength of the mode, a model must be chosen to describe the WGM spectral shape. The lineshape of a single WGM is expected to be a Lorentzian:

$$I(f) = \frac{\gamma}{\pi}\left[\frac{A}{1 + (\frac{f-f_0}{\gamma})^2}\right], \tag{3.4}$$

where A is a normalizing factor, f_0 is the central peak frequency, and γ is the peak width.

A problem associated with the FCM is that the WGMs are asymmetrical: they are skewed towards shorter wavelengths (Figure 3.5). One way to describe the observed asymmetric mode shapes is to use a "skewed" Lorentzian function [110]:

$$I(f) = \frac{2A}{\pi\gamma(f)} \left[\frac{1}{1 + 4(\frac{f-f_0}{\gamma(f)})^2} \right], \tag{3.5}$$

where $\gamma(f)$ is a "skewing parameter" that replaces the Lorentzian linewidth, γ, in Eq. (3.5). The $\gamma(f)$ term can take the following form:

$$\gamma(f) = \frac{(1+B)\gamma_0}{1 + Be^{-a(f-f_0)}}, \tag{3.6}$$

where a and B are skewing parameters. When $a = 0$ or $B = 0$, $I(f)$ becomes a pure Lorentzian. The skewed Lorentzian function provides a better model for the experimental data (Figure 3.5), and was therefore used to estimate the mode shifts.

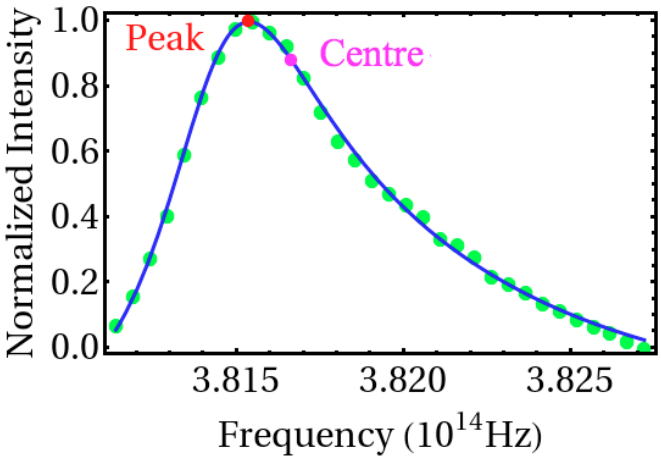

Figure 3.5 – Data for a single WGM peak, fit using a skewed Lorentzian function. The locations of peak and centre values are shown.

In these data, curve fitting methods were found to be difficult for several reasons. First, each peak needs to be cropped from the spectrum, which causes some ambiguity concerning exactly where to set the cropping points. Choosing different cropping points was found to alter the fitting parameters slightly. Second, the spectral sampling rate is fairly poor (Figure 3.5), owing to the 0.1 nm/pixel pitch of the spectrometer. In addition to these issues Eq. (3.6) lacks any basis in theory: it was simply found to fit the data reasonably well.

3.4.2 Fourier Analysis

As an alternative to the CF technique, Fourier transform methods were investigated to measure the WGM mode shifts [66]. FTs are widely employed in signal processing (such as acoustic, optical and seismic data) and have been already applied to optical biosensing methods [111] and biosensing wavelength shift interferometry [112], but they have not yet been used to describe WGM refractometric shifts.

Fourier transform methods take advantage of the periodicity of the whole spectrum. Instead of tracking the shift of single peak over the entire series, here, an overall shift of a WGM spectrum is measured with respect to a reference spectrum (typically the first spectrum in the data series). In the simplest case, the spectral shift can be obtained by finding the frequency shift of the main Fourier component. Alternatively, if the spectra have pure shifts, multiple components can be used. This is the Fourier shift theorem. Accordingly, the phase difference for each Fourier component relates to the shift of the whole spectrum; essentially, shifting a signal by x multiplies the FT by $\mathrm{e}^{-i\omega x}$.

Taking the Fourier transform over a WGM spectrum results in the power and phase data shown in Figure 3.6(a) and (b). The k_F^{th} Fourier component corresponds to the main WGM spectral oscillation. The period of each component is $(f_{\max} - f_{\min})/k_F$, where $f_{\max}$ and $f_{\min}$ are the maximum and minimum frequency in the spectrum. The phase difference, $\Delta\phi$, of the k_F^{th} component corresponds to a WGM shift in real frequency units of

$$\delta f = \Delta\phi \frac{(f_{\max} - f_{\min})}{2\pi k_F}, \tag{3.7}$$

which translates into a wavelength shift of

$$\Delta\lambda = \frac{-4\Delta f c}{(f_{\max} + f_{\min})^2}. \tag{3.8}$$

For a pure shift, each individual component is shifted proportional to k_F, *i.e.*, $\Delta\phi = Ak_F$, where A is a proportionality constant that is a measure of the overall

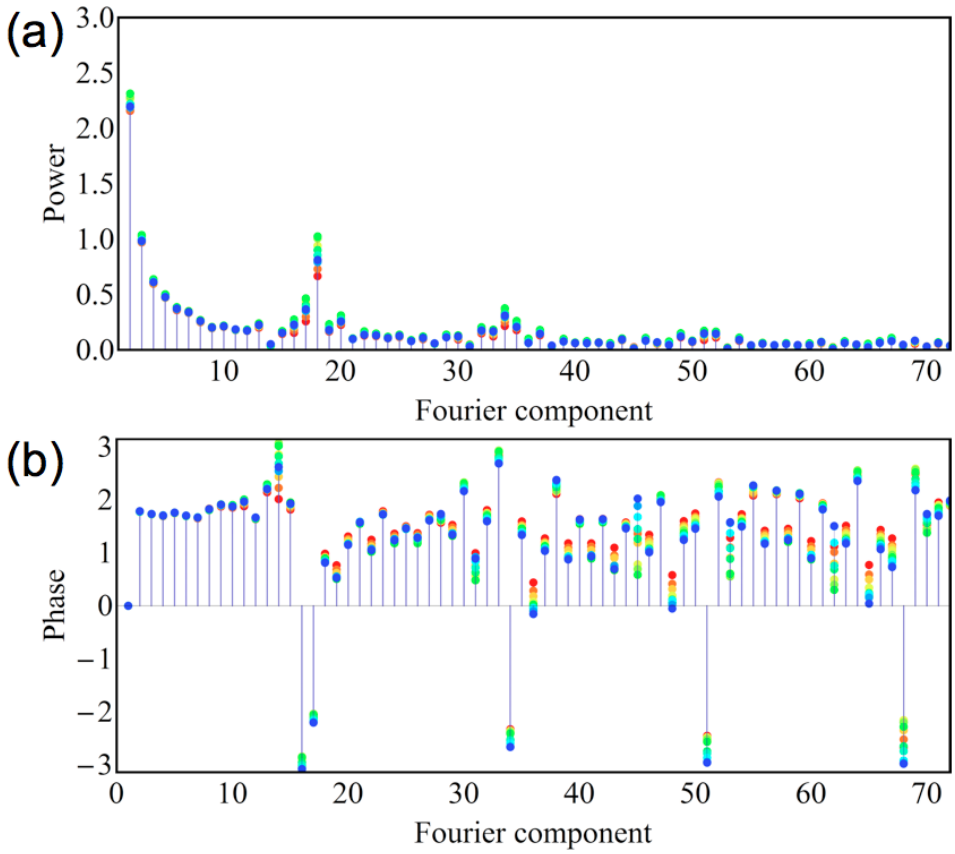

Figure 3.6 – Demonstration of Fourier analysis performed on data from Figure 3.4(a) showing (a) The power spectrum and (b) The phase spectrum.

shift. Since real spectra contain noise, $\Delta\phi$ and k_F may not be well correlated. In such cases, the proportionality constant A can be obtained via a weighted linear fit of a $\Delta\phi$ vs. k_F, where the weight for each component is proportional to its power in the spectrum. The total frequency shift is then given by

$$\delta f = A\frac{(f_{\max} - f_{\min})}{2\pi}, \tag{3.9}$$

which can also be converted into wavelength units. The data analyzed in this chapter used multiple components, whereas the sensorgram and biosensing data in Chapter 4 are analyzed used only the main Fourier component.

3.5 Analysis of experimental data

After calibration and conversion into frequency units, the WGM shifts associated with the spectra shown in Figure 3.4(a) were calculated using three methods: peak picking (PP), curve fitting (CF) and Fourier transform (FT) methods. The peak picking method finds the WGM wavelength shift simply by taking the maximum value of the peak whose shift is to be measured. For the CF case, fits were performed on 7 adjacent peaks in the middle of the spectrum using Eqns. (3.5)–(3.6), where each peak was cropped at the minimum point between adjacent peaks. The FT method used Fourier components, k_F, between 12 and 72. While the choice of filtering is arbitrary, this selection removed high-frequency noise and low-frequency background due to fluorescence that was uncoupled to the cavity.

Experimental WGM wavelength shifts are shown in Figure 3.7 for (i) peak-picking, (ii) curve fitting and (iii) Fourier transform methods. The peak picking and curve fitting methods were performed on a WGM centered at 382 THz. The error bars correspond to one standard deviation from 10 repetitions of a single analysis. The slope (and it's corresponding linear regression error value) of each data set represents the refractometric sensitivity, S, of the capillary.

All three methods show the expected spectral redshift over the narrow change in refractive index investigated. The crude technique of peak picking demonstrated a

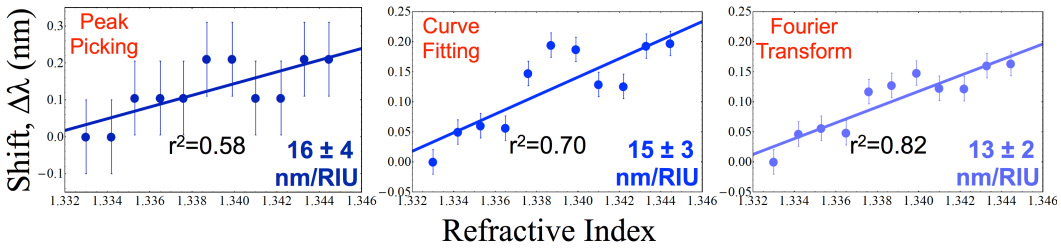

Figure 3.7 – Wavelength shifts for 4-minute exposures, obtained using different methods. Left: peak picking, Middle: curve fitting; Right, Fourier transform. The error bars for each correspond to one standard deviation from 10 repetitions of a single-index index using its corresponding shift analysis.

refractometric sensitivity that was within error of that obtained from the other two methods, albeit, with poor correlation. The FT method gave a better correlation between WGM wavelength shift and solution refractive index than either the curve fitting or peak-picking methods.

The effect of using shorter collection times was investigated using both CF and FT methods.[1] Using short collection times would enable better time resolution for sensorgram analysis. Figure 3.8 shows the spectral shift data for the different collection times, corresponding to SNRs ranging from 300,000 down to 6 (Figure 3.4(c)). These results show that even at a SNR as low as 6 (corresponding to a 1-second exposure time), both the CF and FT methods are able to determine consistent wavelength shifts and give sensitivity values that agree within error. For a SNR value of 0.5, the CF method was unsuccessful. However, even for such a poor SNR, the FT method was able to resolve a the WGM spectral shift and gave a sensitivity comparable to those spectra having much higher SNRs.

The experimental resolution, $\Delta\lambda_{\text{min}}$, is a measure of the ability of the system to measure small spectral shifts. The resolution is proportional to the uncertainty for a given shift measurement. This uncertainty can be obtained in two ways: by repeating a single measurement numerous times, or by examining the deviation of the measured shifts from the linear fit in Figures 3.7 and 3.8 (*i.e.*, by analyzing the residuals). Assuming that the residuals are normally distributed, $\Delta\lambda_{\text{min}}$ can be conservatively estimated as

[1]Here, peak picking analysis methods were left out. For short exposures (low SNR), the peaks can often not be identified and there is no obvious way to pick the peak centre.

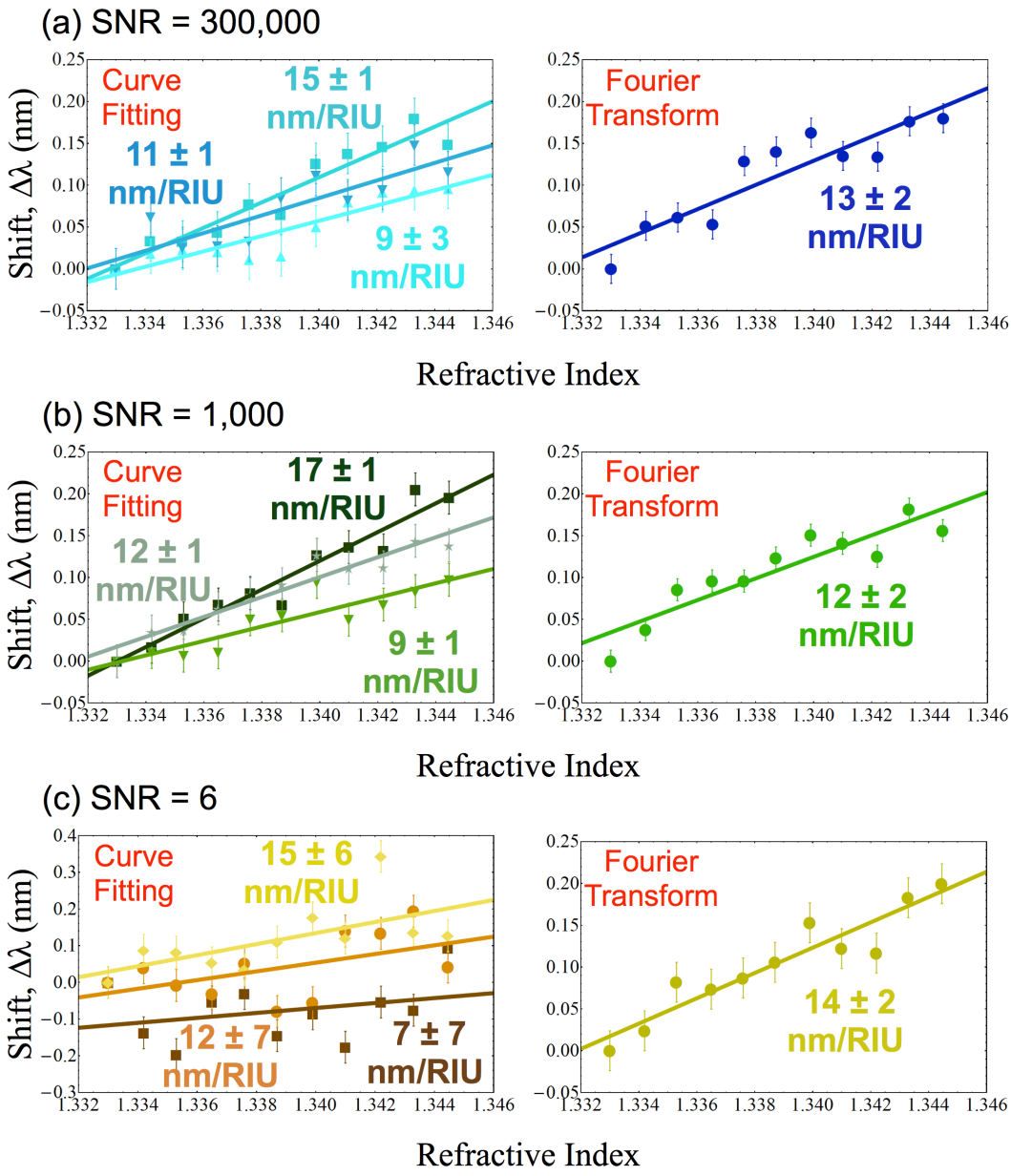

Figure 3.8 – Comparison of curve fitting (left side) and Fourier transform (right side) shift results for different exposure times: (a) SNR of 300000 (4-minute collection) (b) SNR of 1000 (10-second collection) and (c) SNR of 6 (1-second collecution). A SNR of 0.5 did not yield usable results for CF and is not displayed. Each curve fitting result shows 3 different peaks corresponding to the highest, lowest and middle sensitivity values of all 7 peaks fit.

$$\Delta\lambda_{\min} = 3\sigma_{\Delta\lambda_{\min}} = 3\sqrt{\frac{1}{N}\sum_{i=1}^{N}(\Delta\lambda_i - \overline{\Delta\lambda_i})^2}. \tag{3.10}$$

where $\sigma_{\Delta\lambda_{\min}}$ is the standard deviation of the uncertainty in the shift value, N is the number of data points, $\Delta\lambda_i$ is the shift measurement and $\overline{\Delta\lambda_i}$ is the expected value from the linear fit. Finally, the detection limit (for a 3σ or 99.7% confidence interval) is $DL = \Delta\lambda_{\min}/S$.

The experimental sensitivity and resolution for each analysis method are tabulated in Table 3.1. The Fourier transform method gave a better resolution and therefore ultimately a better detection limit as well, and was able to resolve the WGM shifts for exposure times as short as 1-second. The curve fitting method showed a variation in the sensitivity and DL, depending on which peak was chosen; an effect that increased for lower SNRs. The detection limit achieved by both methods is an order of magnitude smaller than the spectrometer pitch.

Table 3.1 – Curve fitting and Fourier transform results for different SNRs. The curve fitting column shows the range of values obtained using different peaks.

SNR	**Curve Fitting**		**Fourier Transform**	
	$\boldsymbol{S}$ **(nm/RIU)**	$\boldsymbol{3\sigma}$ **(pm)**	$\boldsymbol{S}$ **(nm/RIU)**	$\boldsymbol{3\sigma}$ **(pm)**
0.5	NA	NA	12±4	149
6	7±7–15±6	136–230	14±2	57
1000	9±1–17±1	26–46	12±2	59
300000	9±1–15±1	31–65	13±2	65

3.6 Discussion

The ultimate sensitivity and detection limits for the FCM are dependent on the analysis method used to extract the WGM peak shifts. Here, three methods were compared: peak picking, curve fitting, and Fourier transform methods. Peak picking, as expected, gave poor results and was not pursued further. A comparison of the FT and CF methods for quantifying the WGM spectral shifts (for different refractive index fluids in the capillary channel) is important for determining the capabilities of the FCM as a sensor device. Therefore, some further brief discussion is warranted.

As discussed in Sect. 3.3, the capillary WGMs were skewed toward short wavelengths. This led to some difficulty in finding a model for the CF method. Asymmetrical WGMs have been reported in LCORRs as well [34]. The origin of this effect could be related to spiraling WGMs [113]. These are resonances with a non-zero component of the wavevector parallel to the capillary axis. Spiraling modes essentially present a continuum of resonances that are shifted toward shorter wavelengths as a function of spiraling angle, here the mode order is shifted by

$$\lambda = \frac{\pi r \theta^2}{nl}. \tag{3.11}$$

The intensity, $I(\theta)$, of these modes decreases away from the main WGM maximum [113]; however, there is no expression to describe the relationship between θ and $I(\theta)$. Therefore, although the skewed Lorentzian function appears to fit the data well, it lacks theoretical basis.

The Fourier method for finding the spectral shifts was found to be relatively insensitive to noise in the data. This permits a reduction in the collection times, which can be important if sensorgrams are required. For a 1-second exposure time (corresponding to a SNR of 6) the Fourier analysis gave 3σ experimental uncertainties as low as 57 pm. In the biosensing results to be presented in Chapter 4, a collection time of 20 seconds was found to be a good trade-off between SNR and sensorgram temporal resolution.

The parameters summarized in Table 3.1 give a DL approaching 10^{-4} RIU, for the FT shift analysis. This is still two orders of magnitude worse than the DL achievable using LCORRs. However, it is roughly an order of magnitude better than the DL previously obtained for FCMs, where the DL was around 10^{-3} RIU, obtained from CF methods [55]. This result is comparable to recently-published DLs for fluorescent microspheres [64].

There are a few problems associated with the FT method. First, converting the spectra into frequency units is necessary to ensure equal spacing of the modes. This leads to a non-uniform sampling of the spectrum, since the spectrometer samples

evenly in wavelength, which is not compatible with standard FT methods. Therefore, linear interpolation between adjacent data points was used to obtain a uniform frequency spacing of the data. Other more complicated methods do exist for obtaining FT spectra from non-uniformly-sampled data [114], but these were not used here. Secondly, the choice of which Fourier components to include in the analysis is arbitrary. Initially, many Fourier components were selected, *i.e.*, $12 \leq k \leq 72$. However, as the work progressed, only the main Fourier component was selected for measuring the spectral shifts. Choosing only the main component is simply faster and easier than having to deal with phase shifts that can be greater than 2π. Phase shifts greater than 2π lead to a "rollover" problem that, if not individually corrected, can cause large errors in the weighted linear fitting.

Currently, the FT method for obtaining the spectral shifts is automated in a *Mathematica* code that allows for simultaneous batch processing of large numbers of spectral images. This will be important when performing sensorgram analysis for fluids in the FCM, which can result in hundreds or even thousands of spectral images. The FT analysis method was used for all the experimental results in the following chapter.

Chapter 4

Sensorgrams and biosensing

4.1 Initial device characterization: refractometric sensitivity

The refractometric sensitivity of each capillary was measured in order to quantify its suitability for biosensing experiments. For this purpose, a set of preliminary measurements was performed in which the WGMs were measured with methanol, water, and ethanol in the capillary channel. These measurements covered a refractive index range from 1.31446 to 1.35748 in the channel, at a wavelength of 800 nm. This initial characterization was performed using both "traditional" static measurements, and was subsequently repeated in sensorgram format.

4.1.1 Static sensitivity measurements

The refractometric sensitivity of the FCMs was measured by pumping solutions of methanol ($n = 1.31446$), deionized water ($n = 1.32861$) and ethanol ($n = 1.35748$) through the capillary channel. For static measurements, each solution was pumped into the capillary and a single 60-second exposure was taken. The spectra were calibrated as described in Sect. 2.2.2, and the mode shifts were then measured using FT methods described in Sect. 3.4.2, For these measurements, only the main component was used. Figure 4.1 shows the refractometric sensitivity of a representative

sample capillary, for both WGM polarizations. The sensitivity was 15 nm/RIU and 8 nm/RIU for the TM and TE modes, respectively. These sensitivities were typical of successful capillaries prepared using the methods described in Chapter 2.

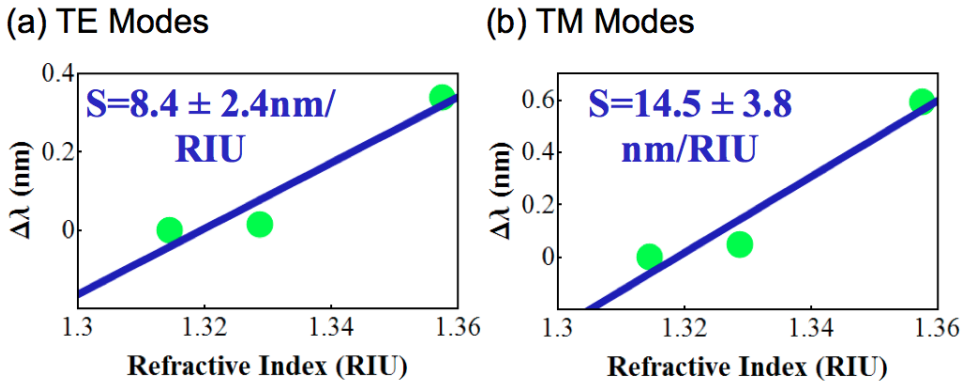

Figure 4.1 – Average refractometric sensitivity for (a) TE modes and (b) TM modes. Data was obtained by pumping methanol, water and ethanol through the capillary channel and taking 60 second exposures for each species. The apparent nonlinearity in the 3 data points is, in fact, consistent with calculations using Eqns. (1.27)–(1.30), which showed that the structure becomes more sensitive at higher refractive index. The error bars on each point are present, however smaller than point size.

4.1.2 Sensorgram sensitivity measurements

For the sensorgram analyses, the following steps were taken. First, 20-second exposures were obtained continuously while each solution was pumped through the capillary (the capillary was different than the one used in the previous section). The total time interval between each spectral image was 30-seconds, since there was a 10 second break for saving the image and resetting the spectrometer for the subsequent exposure. Next, the spectra were batch-analyzed using the methods previously described. The Fourier component corresponding to the main WGM oscillation was used to measure the spectral shifts.

The resulting sensorgram clearly showed the WGM spectral shifts as a function of time for different fluids in the capillary channel (Figure 4.2). There are only small fluctuations of the WGM shift over time, with a single fluid inside the channel. The refractometric sensitivity was extracted by averaging the wavelength shifts over the dark blue data points in Figure 4.2 (*i.e.*, with either methanol, water, or ethanol

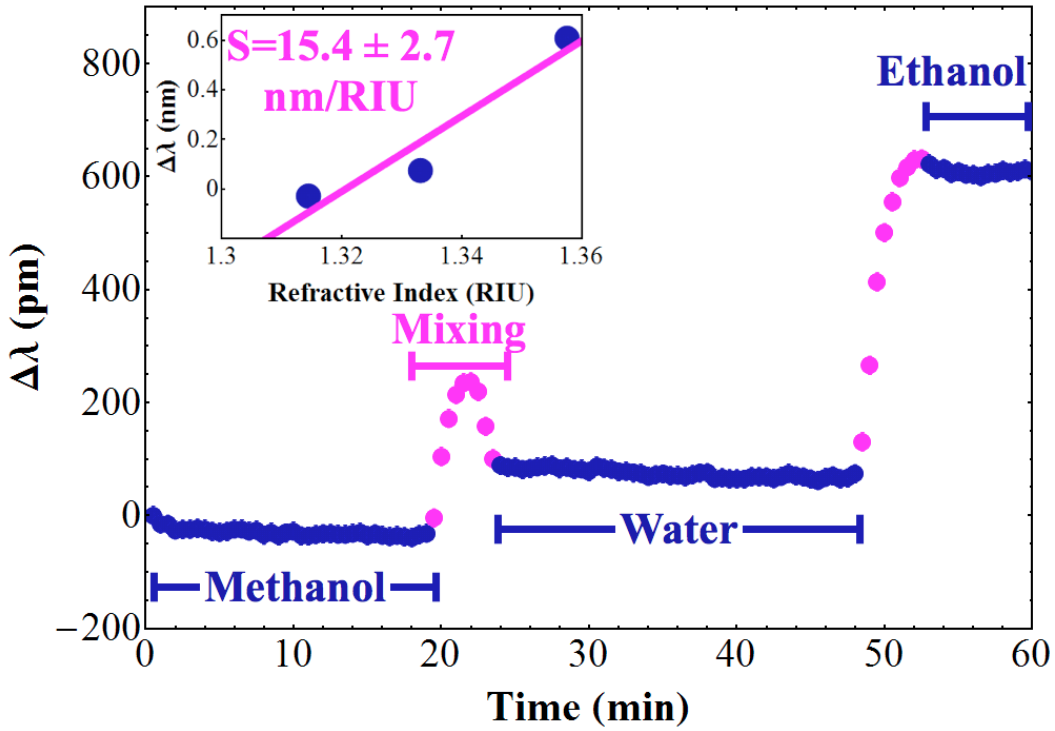

Figure 4.2 – Sensorgram for a 30 micron inner diameter capillary, using TE polarized modes. Each species was pumped through at a rate of 0.002 mL/min and spectra were collected in 20 second intervals and analyzed using Fourier transform. The inset shows the average over the blue data points for methanol, water and ethanol, respectively, and yielded an average sensitivity of 15 nm/RIU. The error bars, although smaller than the data point size represent an experimental shift from 60 spectral images obtained through pumping water through the capillary channel, corresponding to 16.3 pm.

inside the capillary channel). For this capillary, the sensitivity was 15 nm/RIU for TE polarized WGMs. The refractometric sensitivity ranged from 8 nm/RIU to 15 nm/RIU, for all capillaries used in the following biosensing experiments.

The sensorgram shows several additional effects not seen in the static measurements. For example, Figure 4.2 shows a "bump" that occurs during the transition from methanol to water. A smaller bump occurs during the water-ethanol transition. Mixtures of polar liquids such as methanol and water can have a refractive index that is greater than either pure phase. This effect is attributed to the formation of an "associate" phase that forms in water-alcohol mixtures [115].

4.2 Biosensing

The next step was to investigate whether the FCM can be used as a biosensing device. This was attempted using biotin and streptavidin, as a standard "proof-of-principle" protein binding system. The recipe followed was described in Sect. 2.3.2. Briefly, the channel surface was first functionalized with amine groups using 3-aminopropyltrimethoxysilane (APTMS) in 90% methanol + 10% deionized water solution (Figure 4.3). After a set of rinsing steps (see Experimental Sect. 2.3.2), a phosphate buffer saline (PBS) solution was then pumped into the capillary as an initial baseline measurement. This was immediately followed by a solution of BSA-biotin in PBS and another PBS baseline measurement. Finally, streptavidin in a PBS solution was pumped into the channel, followed by a final PBS rinse.

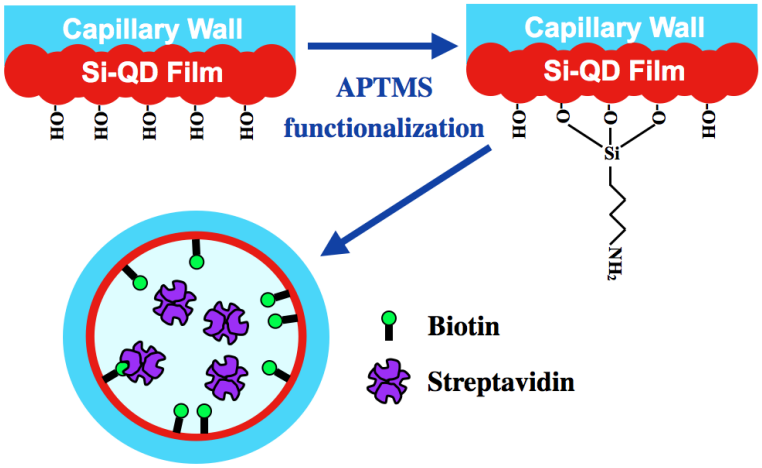

Figure 4.3 – Diagram illustrating binding of biotin to the capillary wall using an amine linker, followed by the subsequent attachment of streptavidin.

4.2.1 Static biosensing experiments

Static biosensing experiments were performed first. In these experiments, each solution was pumped into the capillary, the pumping was stopped, and a 120-second spectrum was taken. All spectra were collected with the pure buffer solution in the capillary, so that any spectral shifts could be attributed to protein binding on the capillary wall. The spectral shifts were measured by Fourier analysis, using only the

main component of the WGM spectrum.

The first biosensing experiment yielded encouraging results (Figure 4.4(a)). For this sample (hereafter referred to as Static I), a 42 ± 23 pm shift was observed after the biotin solution had been pumped through the capillary. This shift corresponds to measurements taken with only pure PBS in the capillary, before and after biotin had been injected. A subsequent shift of 81 ± 23 pm was observed after streptavidin had been pumped through the capillary (again, the shift corresponds to measurements with only pure PBS in the channel).

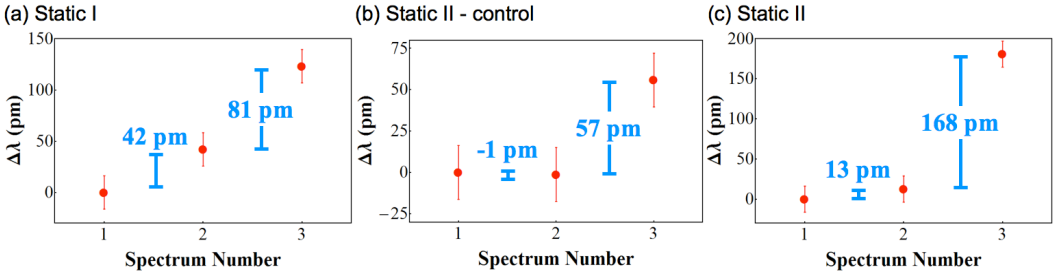

Figure 4.4 – Preliminary static biosensing results. Each species was pumped through the capillary, the pumping was stopped and each spectra was obtained from a 120-second exposure. For all the shifts, only buffer was in the capillary. (a) First biosensing result (Static I), shift was 42 ± 23 pm; and after streptavidin was 81 ± 23 pm. (b) Preliminary control experiment in which APTMS was not pumped through the capillary (Static II-control). The shift before and after biotin was -1 ± 23 pm; before and after streptavidin was 57 ± 23 pm. (c) Biosensing (Static II) using the same capillary in (b), where the surface was functionalized using APTMS. Shift before and after biotin was 13 ± 23 pm; before and after streptavidin was 168 ± 23 pm.

A control measurement (Static II - control) was performed to verify whether biotin and streptavidin had indeed bound the the FCM channel. Here, the surface was not initially functionalized with APTMS. This corresponds to the recipe given in Sect. 2.3.2, except without Step 2. The results are shown in Figure 4.4(b). There was no observable shift for biotin binding; however, although the error is comparatively large, there was a +57± 23 pm shift for the case of streptavidin. This implies the possibility of non-specific binding of streptavidin to the capillary channel.

The same capillary was subsequently functionalized and tested for biosensing (Static II). After the capillary was cleaned with copious amounts of hot water, methanol, ethanol and isopropanol, the surface was functionalized with APTMS. The WGM wavelength shifts for biotin and streptavidin attachment in Static II

were greater than those observed prior to functionalization (Figure 4.4(c)). Here, the shift was 13 ± 23 pm for biotin and 168 ± 23 pm for streptavidin.

4.2.2 Sensorgram biosensing experiments

The initial static experiments suggest that biosensing should be possible using the FCM. However, sensorgrams can provide considerably more data and can help to ascertain the dynamic evolution of the observed wavelength shifts. Three experiments were performed: (i) A full biosensing measurement (Sensorgram-I); (ii) a control in which the FCM was not functionalized (Sensorgram-II); and (iii) a control in which a pre-mixed solution of biotin and streptavidin was pumped into a pre-biotinylated capillary (Sensorgram-III). For Sensorgram II, the recipe in Sect. 2.3.2 was followed, without Step 2. For Sensorgram III, same recipe was followed as before, except that Step 9 consisted of a pre-mixed solution of biotin and streptavidin, rather than streptavidin only (as described in Sect. 2.3.2).

Full biosensing sensorgram

Considerably more data is obtained in the sensorgram (Figure 4.5), as compared to the static measurements in the previous section. For Sensorgram-I (full biosensing experiment), a shift of +69 ± 17 pm was observed after APTMS was pumped into the capillary. This is consistent with the formation of an (3-aminopropyl)-siloxane (APS) layer on the channel surface. Both measurements (*i.e.*, before and after APTMS) were made with 90% methanol in the FCM channel. The subsequent cleaning steps (Steps 3-5) are also clearly observable in the sensorgram (Figure 4.5).

The main biosensing features in Sensorgram-I are highlighted in red in Figure 4.5. PBS-1 indicates the "baseline" measurement after functionalization, in which pure PBS solution was pumped into the FCM for 50 minutes (*i.e.*, after the functionalization process but before biotin was pumped into the capillary). The part of the sensorgram labelled PBS-2 (the second set of red data points) corresponded to pure PBS in the capillary, after the biotin binding step. On going from PBS-1 to PBS-2, a wavelength shift of +36 ± 13 pm was observed. This shift is likely due to biotin

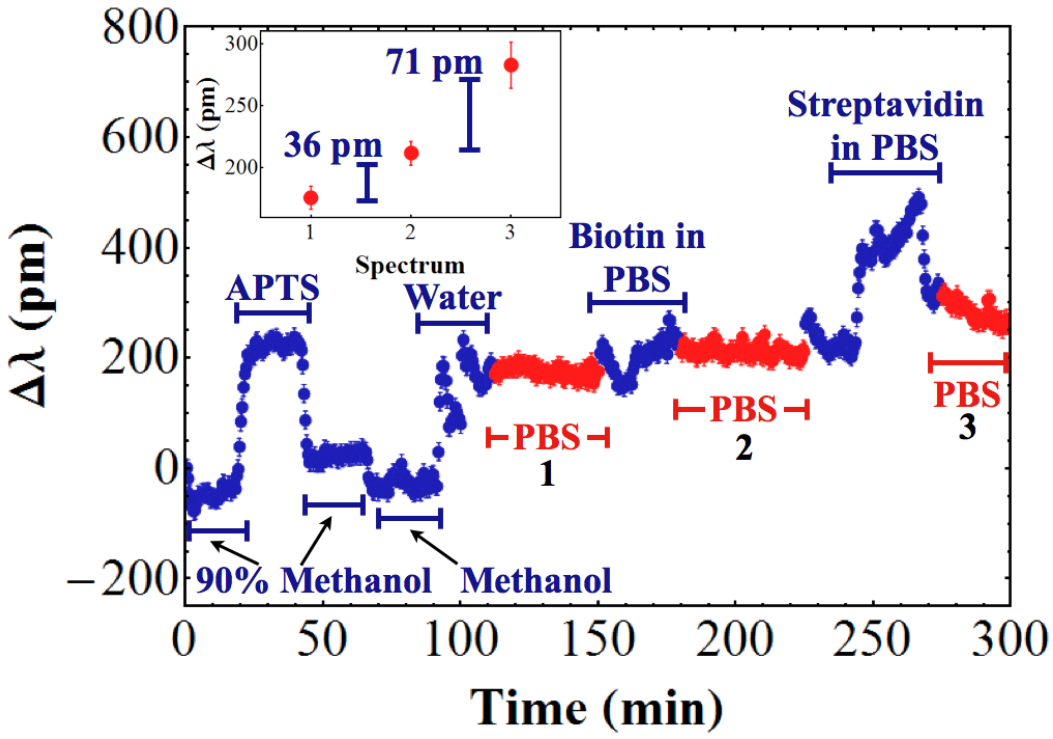

Figure 4.5 – Sensorgram-I: full biosensing sensorgram, starting with the functionalization steps. All solutions were pumped at a rate of 0.002 mL/min. The red regions indicate the buffer being pumped through the capillary. Averaging over the red regions produces the shift plot (inset) showing the expected redshifts both after biotin and streptravidin were pumped into the capillary.

attaching to the APS layer on the channel surface. Next, a solution of streptavidin in PBS was pumped into the capillary for 25 minutes, followed finally by a pure buffer solution (PBS-3). On going from PBS-2 to PBS-3, a further WGM redshift was observed, consistent with the binding of streptavidin. A determination of the wavelength shift was difficult in this case, since the shift (PBS-3) was not "flat" - *i.e.*, there was a gradual blueshift over the remaining time of the experiment. This is suggestive of the gradual removal of streptavidin, as discussed further below.

There are some additional "unexpected" features in the sensorgram that were completely missed in the static measurements. There are two slight dips (*i.e.*, blueshifts) before and after the biotin section and another dip just before the streptavidin section. Also, the streptavidin section never became "flat" (*i.e.*, there was a gradual redshift throughout the entire section). Some possible reasons for these features will be given in Sect. 4.2.2.1.

Control experiment 1: no APTMS

To demonstrate that the functionalization step actually results in binding of specific molecules to the surface (rather than non-specific binding of proteins to the surface regardless whether the amino-linker was present or not), an experiment was performed in which the APS functionalization step was skipped, as was done in the static experiments. The same recipe was followed, including the APTMS "cleaning" steps (90% methanol, deionized water and water), so the only difference was the removal of the functionalization step. This control sensorgram will be referred to as Sensorgram-II.

Control Sensorgram-II was different from the biosensing experiment (Sensorgram-I) in several ways. First, the net average shift after biotin was pumped into the capillary (PBS regions 1 and 2 in Figure 4.6) corresponds to a wavelength shift of -3 $\pm$ 9 pm. Thus, unlike for the previous case, there is no evidence for biotin binding in the control sensorgram. However, despite the lack of functionalization and binding of biotin, streptavidin injection into the capillary did result in a shift of +159 $\pm$ 7 pm. As discussed further below, this is considered evidence that streptavidin can bind to non-biotinylated channel surfaces.

There are also features in the control Sensorgram-II that are similar to those observed in Sensorgram-I. The shifts observed for the 90% methanol, methanol, and water stages, as well as the mixing "bump" between methanol and water, were consistent in both results. There is also a feature at the point where the solution was switched from PBS to biotin in PBS, and another one when the solution was switched to streptavidin. The gradual redshift while streptavidin is pumped through the FCM was once again observed. However, there was no gradual blueshift in PBS stage 3.

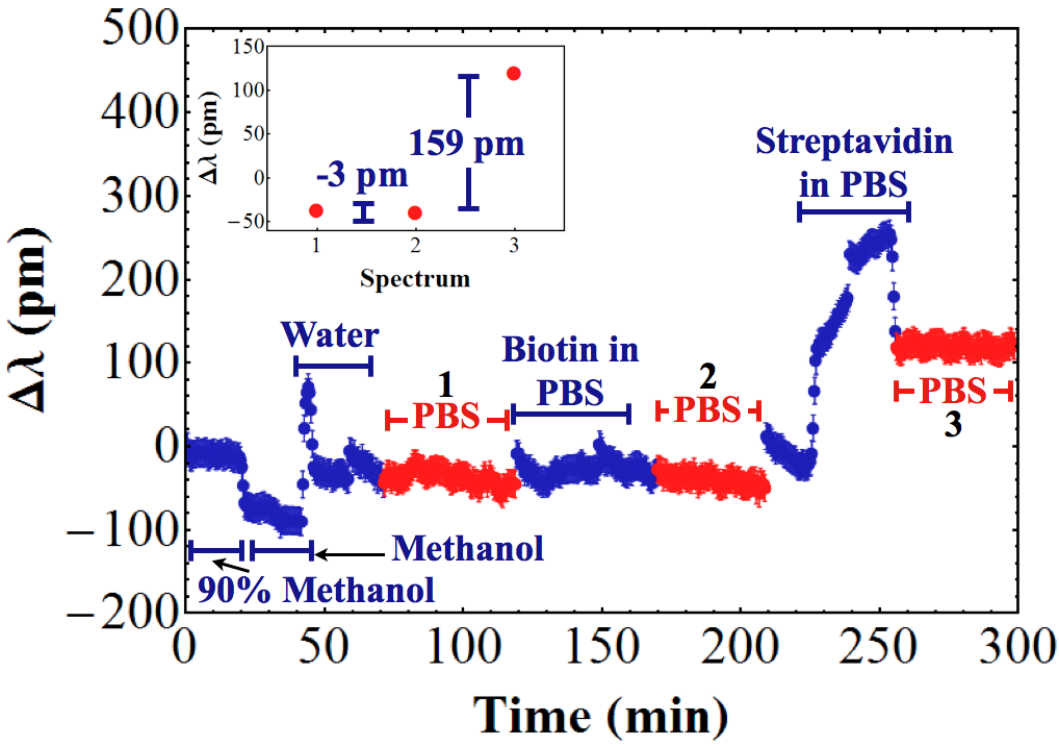

Figure 4.6 – Sensorgram-II: the control experiment, without functionalization using APTMS. All solutions were pumped at a rate of 0.002 mL/min. The red regions indicate the buffer being pumped through the capillary. Averaging over the red regions produces the shift plot (inset) showing shifts both after biotin and streptravidin.

Control experiment 2: biotin followed by a pre-mixed solution of biotin and streptavidin

A second control experiment (Sensorgram-III) was performed where the same initial steps as in Sensorgram-I were followed to obtain the biotinylated surface. In this case, a premixed solution of biotin and streptavidin was used in Step 9, rather than streptavidin only. This causes biotin and streptavidin to bind in solution, blocking all exposed binding sites and, in theory, preventing streptavidin from binding to the biotinylated capillary surface.

The results of Sensorgram-III are depicted in Figure 4.7, where the main features are highlighted in red. The same initial steps were observed as in the biosensing and the first control experiments (Sensorgrams-I and -II). An initial redshift of 27 ± 7 pm was observed after the APS functionalization of the SiO_2. A slight blueshift of -21 ± 6 pm was observed after biotin was pumped into the capillary, although this

feature rides on a gradually blueshifting background. In this sensorgram, the most striking difference was the complete absence of an signal associated with the binding of streptavidin.

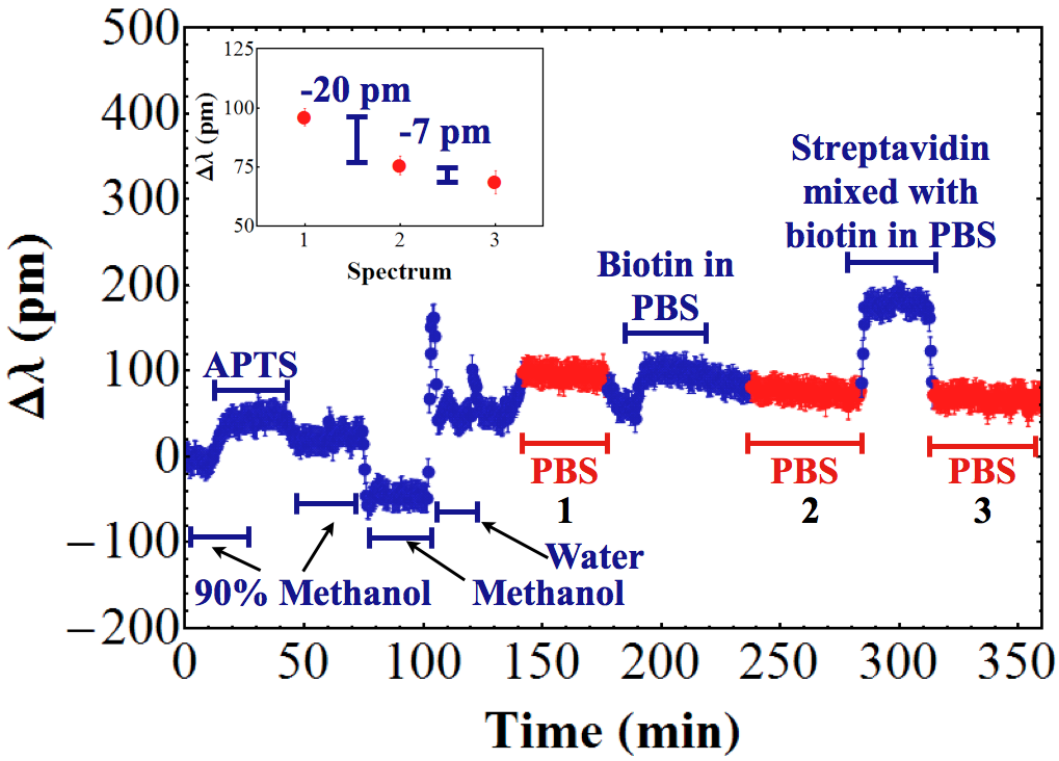

Figure 4.7 – Sensorgram-III: the second control experiment. All solutions were pumped at a rate of 0.002 mL/min. First the surface was functionalized using APTMS and the surface was biotinlyated. Next, a pre-mixed solution of biotin and streptavidin was pumped into the capillary, The red data regions indicate times when only the pure buffer was in the capillary. Averaging over the red regions produces the shift plot (inset), showing blueshifts for both after biotin and after the biotin-streptravidin mixture have been pumped through.

4.2.2.1 Discussion on biosensing results

The experiments performed so far suggest that the FCM could be used as a biosensing device. A summary of all the WGM wavelength shifts for the binding of biotin and streptavidin are presented in Table 4.1. Although the same concentration of each protein was used (and the same concentration of APTMS for the functionalization layer), there are variations in the magnitude of the shifts for each experiment, owing to the different sensitivity and detection limit of each fabricated capillary.

Table 4.1 – Results summary of the WGM shifts for each biosensing experiment.

Experiment	Biotin Shift (pm)	Streptavidin Shift (pm)
Static-I	42 ± 23	81 ± 23
Static-II (control)	-1 ± 23	57 ± 23
Static-II	13 ± 23	168 ± 23
Sensorgram-I: Biosensing	36 ± 13	71 ± 21
Sensorgram-II: Control, no APTMS	-3 ± 10	159 ± 7
Sensorgram-III: Control, biotin followed by biotin/streptavidin mixed	-21 ± 6	-7 ± 6

The WGM shifts for biotin and streptavidin observed in this work can be compared to literature results for other types of WGM-based sensors. In an LCORR, the reported shift was ∼+18 pm for a 1 mg/mL solution of BSA [61]. This was subsequently followed by a shift of an additional ∼+9 pm redshift for a 1.8 μM solution of streptavidin [61]. For a microsphere with a diameter of 300 μm, using the same recipe used in this work, shifts of ∼+21 pm and ∼+19 pm were reported for BSA-biotin and streptavidin, respectively (each with a concentration of 0.01 mg/mL) [49].

The results for the various control samples show the effect of the functionalization layer for the binding of both types of biomolecules. For example, Figure 4.4(b) and Figure 4.6 both show little to no WGM shift for the binding of biotin, in the absence of the functionalization step. This result is consistent with the requirement for an amine end-group for the attachment of biotin, and agrees with the expected non-binding behavior of biotin on a free silica surface [92]. However, streptavidin was more problematic. In Figures 4.4(b) and 4.6, we see positive shifts associated with the binding of streptavidin, even in the absence of the APS step. Thus, streptavidin can apparently bind to the non-functionalized, non-biotinlyated FCM channel surface. This non-specific binding has previously been observed for streptavidin on silica surfaces [116], and is generally non-desirable in a biosensor.

The results suggest that streptavidin can bind non-specifically to the FCM channel, even when the surface is biotinylated. This interpretation is consistent with the following evidence:

- The redshift of the WGM spectrum does not "stop" or saturate over the 25–30 minutes during which the streptavidin was pumped through the capillary (Figures 4.5 and 4.6). Since biotin and streptavidin have an extremely high affinity for each other, the long reaction times observed here are consistent with non-specific binding (either to the APS-functionalized surface, or resulting from increasing thickness of the streptavidin layer).

- The gradual WGM blueshift observed when PBS solution was pumped into the capillary, after the streptavidin step (Figure 4.5). This suggests a gradual removal of non-specifically bound streptavidin from the surface.

- The binding of streptavidin may have been blocked when the streptavidin solution was premixed with BSA-biotin (Figure 4.7).

- Using methods from Refs. [61] and [49], the surface density for biotin and streptavidin for Sensorgram-I was calculated to be 18% and 24%, respectively. This calculated surface coverage suggests that there is more streptavidin on the surface than biotin, some of which must therefore be non-specifically bound.

The problem of non-specific binding of streptavidin (to the functionalized silica) could be minimized via one of several different methods. Increasing the concentration of biotin bound to the surface (*i.e.*, by pumping the biotin solution through the channel for a longer time or by increasing the solution concentration of biotin) could minimize the electrostatic binding of streptavidin to the non-biotinylated surface. [117]. Alternatively, a longer washing step (in PBS buffer) could help remove biotin or streptavidin molecules, that are not strongly bound to the surface [92]. Another method is to sonicate the sample after streptavidin binding [117], however, this was not possible in the current setup.

The chemical stability of the functionalization layer is important to ensure the reliability and repeatability of the biosensing action. Here, a lack of chemical stability means that some APS molecules can be removed from the silica surface. Figure 4.7 shows a gradual WGM blue-shift throughout much of the sensorgram. This could be a result of biotin (and possibly APS) being removed from the channel surface. This behavior was observed in other experiments (not shown) which were ultimately deemed unsuccessful.

Creating a smooth, chemically stable APS layer is highly dependent upon the reaction conditions [93]. The reaction conditions include the concentration of water, the concentration of APTMS, the type of solvent used for the APTMS solution, the rinsing procedures and drying methods, the temperature of reaction, and the reaction time [92, 93, 95–98]. The hydrolysis reaction of APTMS is self-catalyzed, but water can be used as a catalyst to increase the reaction rate. However, an overabundance of water results in a non-stable APS layer, while a deficiency of water will result in the formation of an incomplete APS monolayer [93]. Therefore, one reason that the gradual underlying blueshift observed throughout Figure 4.7 was not observed in the previous sensorgram experiments may be that the composition of the stored 90% methanol/10% water solution may have changed slightly over time, due to evaporation of methanol. For future experiments, the methanol-water solution should be mixed before each experiment.

The structure of the APS layer can strongly affect the protein binding. The bonding geometry is dependent on the reaction conditions for APTMS (as listed in the previous paragraph) [93,95–98]. The desired surface consists of aminosilane layers covalently bound to the silica channel, as shown in Figure 1.14 and Figure 4.8(a). However, some hydrogen-bonding of the silane molecules on the surface can also occur Figure 4.8(b)–(e) [98]. Hydrogen bonds are weak, so those APS molecules can easily be removed from the surface. This could also explain the blue-shift in region PBS-2 of Figure 4.7. Other bonding geometries, such as one in which the amine group is also attached to the surface (Figure 4.8(b)), or one in which the silane group could be pointing away from the surface (Figure 4.8(e)), would inhibit

biotinylation [95].

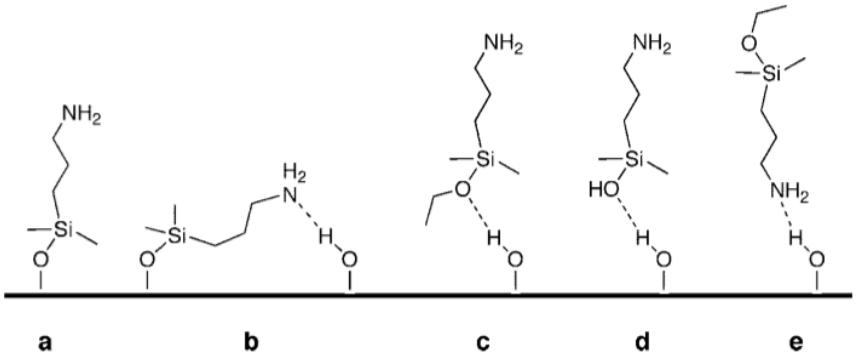

Figure 4.8 – Different possible conformations of APTES on a silicon oxide surface. Reproduced from Ref. [98].

Future experiments could improve the biosensing experiments and reduce the non-specific binding of streptavidin by changing the functionalization reaction conditions. This can help to increase the stability of the APS layer and create the desired bonding geometry. Specifically this could be achieved by curing the APS surface at elevated temperatures [96], changing the APTMS reaction solvent from methanol-water to anhydrous toluene [93], or increasing the reaction time [98]. Improving the stability and bonding geometry of the functionalization layer should permit a wider range of biosensing experiments to be performed.

Chapter 5

Conclusions and outlook

This work has demonstrated that the fluorescent core microcapillary can be used as an inexpensive and microfluidic-compatible optical biosensor. Improved data analysis techniques have allowed for much smaller achievable detections limits and shorter collections times. This permitted the development of sensorgram analysis using the FCM structures. Finally, biosensing experiments were performed using the biotin-streptavidin binding system. The results indicated several benefits and issues associated with this type of biosensor device.

5.1 Summary

Microcapillary resonators were fabricated using a solution-based method to create a fluorescent QD coating on the inner walls of fused silica tubing. The QD film in the FCM supported the development of whispering gallery mode resonances, whose electric field samples the capillary channel. The resonances appear as sharp maxima in the fluorescence spectra emitted by the QDs embedded in the channel surface. When fluids were pumped into the capillaries, the resonances shifted as a result of the fluid refractive index. The first part of this work looked at these capillaries (FCMs) in terms of their potential use as an optical biosensor. The sensitivity and detection limits were investigated, and methods were developed to achieve the best values. By making the detection limit as small as possible, one has the best chance

of successful detection of biomolecules binding to the channel surface.

The second part of this thesis extended the work to the development of sensorgram analysis, rather than the "static"-type measurements that had been used previously. This permits a dynamic analysis of events in the capillary channel, which, as the last stage of the work showed, is important for interpreting the results. Finally, the first attempts at biosensing with these structures were made, using the biotin-streptavidin system because of its high affinity and relatively well-understood binding chemistry. The results suggest that both biotin and streptavidin can be detected when they bind to the FCM channel surface, but that the binding of streptavidin can be at least partly non-specific. The amine functionalization layer seems to be especially important and sensitive to the preparation conditions.

5.1.1 Analysis methods and detection limits

Different data analysis techniques were employed to investigate the sensor performance, by analyzing the spectra obtained with different solutions inside the capillary. Eleven different solutions consisting of sucrose dissolved in water were used, corresponding to a refractive index range of 1.333–1.344. The work compared three different methods for finding the WGM wavelength shifts: (i) peak picking, (ii) curve fitting, and (iii) Fourier transform methods. Here, spectra were obtained in 240-second exposure times. The sensitivity for all three methods was obtained by measuring the slope of a wavelength shift *vs*. refractive index graph. Sensitivities of 16 nm/RIU, 15 nm/RIU, and 13 nm/RIU were extracted for peak picking, curve fitting, and Fourier methods, respectively.

The curve fitting and Fourier methods for finding the wavelength shifts were further compared using different SNRs, ranging from 300000 (240-second exposure) to 0.5 (0.1-second exposure). The experimental sensitivity and 3σ experimental resolution were obtained for the same range of refractive index (1.333–1.344). The FT method gave better (*i.e.*, lower) detection limits, especially when the SNR was low. The CF method resulted in a range of sensitivity and resolution values depending on which peak was chosen for analysis.

The results obtained by comparing the CF and FT methods for measuring the wavelength shift gave insight into the ultimate detection limits for the FCM, when analyzed with a standard spectrometer with a 0.1 nm-per-pixel pitch. The experimental resolution obtained by both methods is an order of magnitude smaller than the spectrometer pitch. For the shorter data collection times, the FT method resulted in DL approaching 10^{-4} RIU and CF methods had detection limits around 10^{-3} RIU. Thus, the FT method was used in the subsequent analyses.

5.1.2 Sensorgrams and biosensing

Before each biosensing experiment, the refractometric sensitivity was determined for each fabricated FCM using both static and sensorgram analysis. The refractometric sensitivity measurement consisted of pumping methanol, water and ethanol solutions into the capillary channel. For the sensorgram analysis, as each solution was pumped into the FCM, spectra were obtained continuously in 20-second exposure intervals. The sensitivity of all capillaries used in the biosensing experiments ranged from 8–15 nm/RIU.

The biotin-streptavidin protein binding system was used as a proof-of-principle biosensing mechanism for the FCM. The surface was initially functionalized using an amine linker in a multi-step process. This was followed by pumping PBS solutions containing biotin and streptavidin, while all shift measurements were made with only pure PBS in the channel. Initial static measurements yielded results that showed a 42 $\pm$ 23 pm and 81 $\pm$ 23 pm shift, corresponding to the binding of biotin and streptavidin, respectively (Static-I). An initial static control measurement was performed in which APTMS was not pumped through the capillary (Static-II control). A greater shift was observed for both biotin and streptavidin when the surface was functionalized.

The biotin-streptavidin biosensing experiments were also performed in sensorgram format for three different experiments: (i) full biosensing (Sensorgram-I); (ii) control without APTMS step, *i.e.*, no functionalization, (Sensorgram-II); and (iii) a control in which biotin was first pumped into the capillary, followed by a pre-mixed

solution of biotin and streptavidin (Sensorgram-III). The full biosensing experiment resulted in wavelength shifts for biotin and streptavidin of 36 ± 13 pm and 71 ± 21 pm, respectively, comparable to the initial static shift measurements. The first control did not yield any WGM shift associated with the binding of biotin; however, streptavidin still yielded a redshift of 159 ± 7 pm. This suggests the binding of streptavidin to the silica surface, even in the absence of a pre-bound biotin layer. The second control experiment gave no observable redshift when the streptavidin solution had been "blocked" with pre-mixed biotin. The mixture may have prevented the binding of streptavidin by blocking all binding clefts with biotin.

Overall, the results are consistent with the successful detection of biotin and streptavidin binding to the FCM surface. Thus, this represents a potential new optical sensor architecture (a capillary with the fluorescent channel coating). The work also identified several issues that could be improved in future study, especially relating to the functionalization chemistry and the experimental measurement system itself.

5.2 Future study

The work demonstrated here indicated a number of avenues for refining and improving the devices in order to make better and faster measurements. The possible improvements are:

- A more reliable method to create the FCM. The success rate for sample fabrication in this work was likely too low to be practical, with just a few successfully coated capillaries from hundreds that were prepared. One possibility might be to employ a "blow-through" method for getting the film to coat the capillary channel more consistently and reliably. This would involve blowing inert gas through the capillary after it has been dipped in the precursor solution. The flow rate or pressure might better control the film thickness, and could reduce the amount of precursor solution deposited on the capillary walls prior to annealing. A thinner QD-film on the capillary wall would increase the sensitivity

of the device and might ultimately improve the detection limits of the FCM.

- The wavelength shift measurement method could be better optimized. Currently, the method requires some "hand-analysis" of the Fourier spectra produced from each measurement. This is done in order to (arbitrarily) determine the number of components to accept in the analysis and to make sure that none of the accepted components have a 2π "rollover" problem. Also, the coding is all done in *Mathematica* and would be rather difficult for an inexperienced user to learn.

- Live-time analysis would be better than the batch processing subsequent to the analysis that was done in this work. This would require special software coding of the spectroscopy system.

- A better handle on the functionalization step would be desirable. The APS functionalization is sensitive to the amount of water present, so future work might investigate using APTES or APTMS in an anhydrous toluene solution, since the hydrolysis reaction is self-catalyzed. This will require a re-evaluation of the tubing and adhesives used. Also, studies of the exposure time, and APS concentration, and thermal curing could help make more stable APS layers. Different functionalization procedures, for example using amine-reactive homobiofunctional cross-linker glutaraldehyde, could be also investigated.

- Ideally, a sensor device should be reusable. For the FCM to be reusable, a recipe for removing the pre-existing functionalization layer is needed. One way to do this is to inject piranha solution (a mixture of sulfuric acid and hydrogen peroxide) into the capillary. However, piranha is dangerous and it may not be simple to pump it into the capillary and remove it. An HCl/methanol solution was recently investigated in our group, however this solution reacted with the stainless steel syringes. There are other recipes that could remove any biomolecules present, but not remove the functionalization. For example, White *et al.* used a "multi-ingredient stripping cocktail" (also used in SPR

studies) to remove phage immobilization but preserve the surface functionalization for future biosensing studies [61].

- The experimental setup itself could be considerably improved. The long tube lengths required in the current system require a lengthy pumping time, and make the experiments take up to a whole day for a full run. A better way to inject multiple solutions should be developed, for example by using multiple input connectors, although this does raise an issue of dead volume and mixing. Still, physically exchanging syringes during the experiment should not be the best available option for future work.

Despite these ideas for future improvement, the results presented in this thesis demonstrate that biosensing with FCMs is feasible. This opens the door to a wide range of potential future experiments, including those with more relevant biomaterials. For example, one possible future project is the detection of antibodies in certain food products (*e.g.*, dairy). The great advantage of the FCM structure is its physical robustness, the fact that virtually any fluid can be pumped into the device, and that the functionalization recipes are based on silica, which is one of the most common substrates for biosensing experiments.

Bibliography

[1] A. B. Dahlin, *Plasmonic Biosensors*. Amsterdam, Netherlands: IOS Press, 2012.

[2] D. Erickson, S. Mandal, A. H. J. Yang, and B. Cordovez, "Nanobiosensors: optofluidic, electrical and mechanical approaches to biomolecular detection at the nanoscale," *Microfluidics and Nanofluidics*, vol. 4, no. 1-2, pp. 33–52, 2008.

[3] S. Li, J. Singh, H. Li, and I. A. Banerjee, eds., *Biosensor Nanomaterials*. Weinheim, Germany: Wiley-VCH Verlag GmbH & Co. KGaA, 2011.

[4] A. Merkoçi, ed., *Biosensing using Nanomaterials*. Hoboken, NJ, USA: John Wiley & Sons, Inc., 2009.

[5] P. Wang and Q. Liu, *Biomedical Sensors and Measurement*. Zhejiang University Press, Springer-Verlag Berlin Heidelberg, 2011.

[6] A. F. Collings and F. Caruso, "Biosensors: recent advances," *Reports on Progress in Physics*, vol. 60, pp. 1397–1445, 1997.

[7] L. C. Clark, R. Wolf, D. Granger, and Z. Taylor, "Continuous recording of blood oxygen tensions by polarography," *Journal of Applied Physiology*, vol. 6, no. 3, pp. 189–193, 1953.

[8] S. Vaddiraju, I. Tomazos, D. J. Burgess, F. C. Jain, and F. Papadimitrakopoulos, "Emerging synergy between nanotechnology and implantable biosensors: A review," *Biosensors and Bioelectronics*, vol. 25, pp. 1553–1565, 2010.

[9] B. T. Cunningham, *Label-Free Biosensors: Techniques and Applications*. Cambridge, U.K.: Cambridge University Press, 2009.

[10] N. Jokerst, M. Royal, S. Palit, L. Luan, S. Dhar, and T. Tyler, "Chip scale integrated microresonator sensing systems," *Journal of BioPhotonics*, vol. 2, no. 4, pp. 212–226, 2009.

[11] C. Chao, T. Ling, and L. J. Guo, *Advanced Photonic Structures for Biological and Chemical Detection*, ch. 8: Label-Free Biochemical Sensors Based on Optical Microresonators. New York, NY: Springer, 2009.

[12] X. Fan, I. M. White, S. I. Shopova, H. Zhu, J. D. Suter, and Y. Sun, "Sensitive optical biosensors for unlabeled targets: A review," *Analytica Chimica ACTA*, vol. 620, pp. 8–26, 2008.

[13] M. A. Cooper, "Optical biosensors in drug discovery," *Nature Reviews*, vol. 1, pp. 515–528, 2002.

[14] J. S. Daniels and N. Pourmand, "Label-free impedence biosensors: Opprotunities and challenges," *Electroanalysis*, vol. 19, no. 12, pp. 1239–1257, 2007.

[15] B. Liedberg, C. Nylander, and I. Lunström, "Surface plasmon resonance for gas detection and biosensing," *Sensors and Actuators*, vol. 4, pp. 299–304, 1983.

[16] J. Homola, "Present and future of surface plasmon resonance biosensors," *Analytical and Bioanalytical Chemistry*, vol. 377, no. 3, pp. 528–539, 2003.

[17] P. Pattnaik, "Surface plasmon resonance: Applications in understanding receptor-ligand interaction," *Applied Biochemistry and Biotechnology*, vol. 126, no. 2, pp. 79–92, 2005.

[18] M. A. Cooper, "Label-free screening of bio-molecular interactions," *Analytical and Bioanalytical Chemistry*, vol. 377, pp. 834–842, 2003.

[19] C. Rhodes, S. Franzen, J. P. Maria, M. Losego, L. D. N, B. Laughlin, G. Duscher, and S. Weibel, "Surface plasmon resonance in conducting metal oxides," *Journal of Applied Physics*, vol. 100, p. 054905, 2006.

[20] J. Homola, S. S. Yee, and G. Günter, "Surface plasmon resonance sensors: review," *Sensors and Actuators B: Chemical*, vol. 54, pp. 3–15, 1999.

[21] BiaCORE, "Technology note 1: Surface plasmon resonance." (www.biacore.com), 2001.

[22] I. Abdulhalim, M. Zourob, and A. Lakhtakia, "Surface plasmon resonance for biosensing: a mini-review," *Electromagnetics*, vol. 28, pp. 214–242, 2008.

[23] H.-M. Haake, A. Schütz, and G. Gauglitz, "Label-free detection of biomolecular interaction by optical sensors," *Fresenius' Journal of Analytical Chemistry*, vol. 366, no. 6-7, pp. 576–585, 2000.

[24] BiaCORE (http://www.biocore.com/).

[25] Texas Instruments Group (http://www.ti.com/spr).

[26] BioTuL (http://www.biotul.com/).

[27] A. J. Haes and R. P. Van Duyne, "A unified view of propagating and localized surface plasmon resonance biosensors," *Analytical and Bioanalytical Chemistry*, vol. 379, no. 7-8, pp. 920–930, 2004.

[28] J. M. Perkel, "Surface plasmon resonance (SPR) and other options for label-free detection." Editorial Articles, (http://www.biocompare.com/), March 2011.

[29] B. E. A. Saleh and M. C. Teich, *Fundamentals of Photonics*. Wiley, 2nd ed., 2007.

[30] M. L. Gorodetsky, A. A. Savchenkov, and V. S. Ilchenko, "Ultimate Q of optical microsphere resonators," *Optics Letters*, vol. 21, no. 7, pp. 453–455, 1995.

[31] I. M. White and X. Fan, "On the performance quantification of resonant refractive index sensors," *Optics Express*, vol. 16, no. 2, pp. 1020–1028, 2008.

[32] F. Vollmer and S. Arnold, "Whispering-gallery-mode biosensing: label-free detection down to single molecules," *Nature Methods*, vol. 5, no. 7, pp. 591–596, 2008.

[33] D. W. Vernooy, V. S. Ilchenko, H. Mabuchi, E. W. Streed, and H. J. Kimble, "High-Q measurements of fused-silica microspheres in the near infrared," *Optics Letters*, vol. 23, no. 4, pp. 247–249, 1998.

[34] V. Zamora, A. Díez, M. V. Andrés, and B. Gimeno, "Refractometric sensor based on whispering-gallery modes of thin capillaries," *Optics Express*, vol. 15, no. 19, pp. 12011–12016, 2007.

[35] A. M. Armani, R. P. Kulkarni, S. E. Fraser, R. C. Flagan, and K. J. Vahala, "Label-free, single-molecule detection with optical microcavities," *Science*, vol. 317, no. 5839, pp. 783–787, 2007.

[36] M. L. Gorodetsky and V. S. Ilchenko, "High-Q optical whispering-gallery microresonators: precession approach for spherical mode analysis and emission patterns with prism couplers," *Optics Communications*, vol. 113, pp. 133–143, 1994.

[37] L. Rayleigh, "The problem of the whispering gallery," *Philosphical Magazine*, vol. 20, pp. 115–120, 1910.

[38] M. Born and E. Wolf, *Principles of Optics*. Cambridge University Press, 7th ed., 1999.

[39] D. J. Griffiths, *Introduction to Electrodynamics*. Pearson Addison Wesley, 3rd ed., 1999.

[40] E. Hecht, *Optics*. Addison-Wesley, 4th ed., 2002.

[41] F. L. Pedrotti, L. S. Pedrotti, and L. M. Pedrotti, *Introduction to Optics*. Pearson Prentice Hall, 3rd ed., 2007.

[42] I. Teraoka, S. Arnold, and F. Vollmer, "Perturbation approach to resonance shifts of whispering-gallery modes in a dielectric microsphere as a probe of a surrounding medium," *Optical Society of America B*, vol. 20, pp. 1937–1946, 2003.

[43] A. N. Oraevsky, "Whispering-gallery waves," *Quanutm Electronics*, vol. 32, no. 5, pp. 377–400, 2002.

[44] I. Teraoka and S. Arnold, "Theory of resonance shifts in te and tm whispering gallery modes by nonradial perturbations for sensing applications," *Journal of the Optical Society of America B*, vol. 23, pp. 1381–1389, 2006.

[45] I. Teraoka and S. Arnold, "Whispering-gallery modes in a microsphere coated with a high-refractive index layer: polarization-dependent sensitivity enhancement of the resonance-shift sensor and TE-TM resonance matching," *Journal of the Optical Society of America B*, vol. 24, pp. 653–659, 2007.

[46] I. Teraoka and S. Arnold, "Enhancing the sensitivity of a whispering-gallery mode microsphere sensor by a high-refractive-index surface layer," *Journal of the Optical Society of America B*, vol. 23, pp. 1434–1441, 2006.

[47] I. M. White, H. Oveys, X. Fan, T. L. Smith, and J. Zhang, "Integrated multiplexed biosensors based on liquid core optical ring resonators and antiresonant reflecting optical waveguides," *Applied Physics Letters*, vol. 89, p. 191106, 2006.

[48] I. M. White, H. Oveys, and X. Fan, "Liquid-core optical ring-resonator sensors," *Optics Letters*, vol. 31, pp. 1319–1321, 2006.

[49] F. Vollmer, D. Braun, A. Libchaber, M. Khoshsima, I. Teraoka, and S. Arnold, "Protein detection by optical shift of a resonant microcavity," *Applied Physics Letters*, vol. 80, no. 21, pp. 4057–4059, 2002.

[50] S. Soria, S. Berneschi, M. Brenci, F. Cosi, G. N. Conti, S. Pelli, and G. C. Righini, "Optical microspherical resonators for biomedical sensing," *Sensors*, vol. 11, no. 1, pp. 785–805, 2011.

[51] A. M. Beltaos and A. Meldrum, "Whispering gallery modes in silicon-nanocrystal-coated silica microspheres," *Journal of Luminescence*, vol. 126, pp. 607–613, 2007.

[52] P. Bianucci, J. R. Rodríguez, C. M. Clements, J. G. C. Veinot, and A. Meldrum, "Silicon nanocrystal luminescence couple to wipsering gallery modes in optical fibers," *Journal of Applied Physics*, vol. 105, p. 023108, 2009.

[53] A. Yalçin, K. C. Popat, J. C. Aldridge, T. A. Desai, J. Hryniewicz, N. Chbouki, B. E. Little, O. King, V. Van, S. Chu, D. Gill, M. Anthes-Washburn, M. S. Ünlü, and B. B. Goldberg, "Optical sensing of biomolecules using microring resonators," *IEEE Journal of Slected Topics in Quantum Electronics*, vol. 12, no. 1, pp. 148–155, 2006.

[54] I. M. White, H. Zhu, J. D. Suter, X. Fan, and M. Zourob, "Label-free detection with the liquid core optical ring resonator sensing platform," *Biosensor and Biodetection Methods in Molecular Biology*, vol. 503, pp. 139–165, 2009.

[55] C. P. K. Manchee, V. Zamora, J. W. Silverstone, J. G. C. Veinot, and A. Meldrum, "Refractometric sensing with fluorescent-core microcapillaries," *Optics Express*, vol. 19, pp. 21540–21551, 2011.

[56] D. X. Xu, A. Densmore, A. Delage, P. Waldron, R. McKinnon, S. Janz, J. Lapointe, G. Lopinski, T. Mischki, E. Post, P. Cheben, and J. H. Schmid, "Folded cavity SOI microring sensors for high sensitivity and real time measurement of biomolecular binding," *Optics Express*, vol. 16, pp. 15137–15148, 2008.

[57] V. S. Ilchenko, M. L. Gorodetsky, X. S. Yao, and L. Maleki, "Microtorus: a high-finesses microcavity with whispering-gallery modes," *Optics Letters*, vol. 26, pp. 256–258, 2001.

[58] V. Zamora, A. Díez, M. V. Andrés, and B. Gimeno, "Cylindrical optical microcavities: Basic properties and sensor applications," *Photonics and Nanostructures - Fundamentals and Applications*, vol. 9, pp. 149–158, 2011.

[59] J. D. Suter, I. M. White, H. Zhu, H. Shi, C. W. Caldwell, and X. Fan, "Label-free quantitative dna detection using the liquid core optical ring resonator," *Biosensors and Bioelectronics*, vol. 23, no. 7, pp. 1003–1009, 2008.

[60] H. Zhu, I. M. White, J. D. Suter, P. S. Dale, and X. Fan, "Analysis of biomolecule detection with optofluidic ring resonator sensors," *Optics Express*, vol. 15, no. 15, pp. 9139–9146, 2007.

[61] H. Zhu, I. M. White, J. D. Suter, and X. Fan, "Phage-based label-free biomolecule detection in an opto-fluidic ring resonator," *Biosensors and Bioelectronics*, vol. 24, pp. 461–466, 2008.

[62] J. T. Gohring, P. S. Dale, and X. Fan, "Detection of HER2 breast cancer biomarker using the opto-fluidic ring resonator biosensor," *Sensors and Actuators B: Chemical*, vol. 146, pp. 226–230, 2010.

[63] I. M. White, H. Zhu, J. D. Suter, N. M. Hanumegowda, H. Oveys, M. Zourob, and X. Fan, "Refractometric sensors for lab-on-a-chip based on optical ring resonators," *IEEE Sensors Journal*, vol. 7, pp. 28–35, 2007.

[64] S. Pang, R. E. Beckham, and K. E. Meissner, "Quantum dot-embedded microspheres for remote refractive index sensing," *Applied Physics Letters*, vol. 92, no. 22, p. 221108, 2008.

[65] P. Bianucci, C. Rodríguez, J Rand Clements, C. M. Hessel, J. G. C. Veinot, and A. Meldrum, "Whispering gallery modes in silicon nanocrystal coated microcavities," *Physica Satus Solidi A*, vol. 206, pp. 973–975, 2009.

[66] J. W. Silverstone, S. McFarlane, C. P. K. Manchee, and A. Meldrum, "Ultimate resolution for refractometric sensing with whispering gallery mode microcavities," *Optics Express*, vol. 20, pp. 8284–8295, 2012.

[67] L. Pavesi and R. Turan, eds., *Silicon Nanocrystals: Fundamentals, Synthesis and Applications*. Wiley-VCH Verlag GmbH & Co. KGaA, 2010.

[68] L. E. Brus, P. F. Szajowski, W. L. Wilson, T. D. Harris, S. Schuppler, and P. H. Citrin, "Electronic spectroscopy and photophysics of Si nanocrystals: relationship to bulk c-Si and porous Si," *Journal of the American Chemical Society*, vol. 117, no. 10, pp. 2915–2922, 1995.

[69] J. R. Rodríguez, J. G. C. Veinot, P. Bianucci, and A. Meldrum, "Whispering gallery modes in hollow cylindrical microcaities containing silicon nanocrystals," *Applied Physics Letters*, vol. 92, p. 131119, 2008.

[70] A. Boleininger, T. Lake, S. Hami, and C. Vallance, "Whispering gallery modes in standard optical fibres for fibre profiling measurements and sensing of unlabelled chemical species," *Sensors*, vol. 10, no. 3, pp. 1765–1781, 2010.

[71] C. P. K. Manchee, "Refractometric sensing with fluorescent-core microcapillaries," Master's thesis, University of Alberta, Edmonton, Alberta, Canada, September 2011.

[72] C. M. Hessel, E. J. Henderson, and J. G. C. Veinot, "Hydrogen silsesquioxane: A molecular precursor for nanocrystalline Si-SiO_2 composites and freestanding hydride-surface-terminated silicon nanoparticles," *Chemistry of Materials*, vol. 18, no. 26, pp. 6139–6146, 2006.

[73] S. V. Gaponenko, *Optical Properties of Semiconductor Nanocrystals*. Cambridge University Press, 1998.

[74] M. Fox, *Optical Properties of Solids*. Oxford University Press, 2nd ed., 2010.

[75] Z. Lu, D. J. Lockwood, and J. M. Baribeau, "Quantum confinement and light emission in SiO_2/Si superlattices," *Nature*, vol. 378, pp. 258–260, 1995.

[76] A. G. Nassiopoulos, S. Grigoropoulos, and D. Papadimitriou, "Electroluminescent device based on silicon nanopillars," *Applied Physics Letters*, vol. 69, pp. 2267–2269, 1996.

[77] M. Fox, *Quantum Optics: An Introdution*. Oxford University Press, 2010.

[78] A. P. Alivisatos, "Semiconductor clusters, nanocrystals and quantum dots," *Science*, vol. 271, no. 5251, pp. 933–937, 1996.

[79] A. P. Alivisatos, "Perspectives on the physical chemistry of semiconductor nanocrystals," *Journal of Physical Chemistry*, vol. 100, no. 31, pp. 13226–13239, 1996.

[80] D. S. English, L. E. Pell, Z. Yu, P. F. Barbara, and B. A. Korgel, "Size tunable visible luminescence from individual organic monolayer stabilized silicon nanocrystal quantum dots," *Nano Letters*, vol. 2, no. 7, pp. 681–685, 2002.

[81] L. Pavesi, "Silicon-based light sources for silicon integrated circuits," *Advances in Optical Technologies*, vol. 2008, 2008.

[82] L. T. Canham, "Gaining light from silicon," *Nature*, vol. 408, pp. 411–412, 2000.

[83] R. J. Walters, J. Kalkman, A. Polman, H. A. Atwater, and M. J. A. de Dood, "Photoluminescence quantum efficiency of dense silicon nanocrystal ensembles in SiO_2," *Physical Review B*, vol. 73, no. 13, p. 132302, 2006.

[84] Y. Q. Wang, G. L. Kong, W. D. Chen, H. W. Diao, C. Y. Chen, S. B. Zhang, and X. B. Liao, "Getting high-efficiency photoluminescence from Si nanocrystals in SiO_2 matrix," *Applied Physics Letters*, vol. 81, pp. 4174–4176, 2002.

[85] T. V. Torchynska, A. D. Cano, M. M. Rodriguez, and L. Y. Khomenkova, "Hot carriers and excitation of Si/SiO_x interface defect photoluminescence in Si nanocrystallites," in *Physica B: Condensed Matter*, vol. 340-342, pp. 1113–1118, 22nd Annual International Conference on Defects in Semiconductors, 2003.

[86] J. Li, W. Tan, K. Wang, D. Xiao, X. Yang, X. He, and Z. Tang, "Ultrasensitive optical DNA biosensor based on surface immobilization of molecular beacon by a bridge structure," *Analytical Sciences*, vol. 17, no. 10, pp. 1149–1153, 2001.

[87] C. Shi, S. Mehrabani, and A. M. Armani, "Leveraging bimodal kinetics to improve detection specificity," *Optics Letters*, vol. 37, no. 10, pp. 1643–1645, 2012.

[88] J. Zempleni, S. S. Wijeratne, and Y. I. Hassan, "Biotin," *Biofactors*, vol. 35, no. 1, pp. 36–46, 2009.

[89] Toxnet: Toxicology Data Network (http://toxnet.nlm.nih.gov/).

[90] C. L. Smith, J. S. Milea, and G. H. Nguyen, "Immobilization of nucleic acids using biotin-strept(avidin) systems," *Topics in Current Chemistry*, vol. 261, pp. 63–90, 2005.

[91] A. Holmberg, B. A, O. Nord, M. Lukacs, J. Lundeberg, and M. Uhlén, "The biotin-streptavidin interaction can be reversibly broken using water at elevated temperatures," *Electrophoresis*, vol. 26, no. 3, pp. 501–510, 2005.

[92] N. A. Lapin and Y. J. Chabal, "Infrared characterization of biotinylated silicon oxide surfaces, surface stability, and specific attachment of streptavidin," *Journal of Physical Chemistry B*, vol. 113, no. 25, pp. 8776–8783, 2009.

[93] J. A. Howarter and J. P. Youngblood, "Optimization of silica silanization by 3-aminopropyltriethoxysilane," *Langmuir*, vol. 22, no. 26, pp. 11142–11147, 2006.

[94] S. Gilles, "Chemical modification of silicon surfaces for the application in soft lithography," tech. rep., Institute of Bio- and Nanoystems (IBN), Biolectronics (IBN-2), 2007.

[95] E. T. Vandenberg, L. Bertilsson, B. Liedberg, K. Uvdal, R. Erlandsson, H. Elwing, and I. Lundström, "Structure of 3-aminopropyl triethoxy silane on silicon oxide," *Journal of Colloid and Interface Science*, vol. 147, no. 1, pp. 103–118, 1991.

[96] R. M. Pasternack, S. R. Amy, and Y. J. Chabal, "Attachment of 3-(aminopropyl)triethoxysilane on silicon oxide surfaces: dependence on solution temperature," *Langmuir*, vol. 24, no. 22, pp. 12963–12971, 2008.

[97] N. Aissaoui, L. Bergaoui, J. Landoulsi, J. F. Lambert, and S. Boujday, "Silane layers on silicon surfaces: mechanism of interaction, stability and influence on protein absorption," *Langmuir*, vol. 28, no. 1, pp. 656–665, 2012.

[98] E. A. Smith and W. Chen, "How to prevent the loss of surface functionality derived from aminosilanes," *Langmuir*, vol. 24, no. 21, pp. 12405–12409, 2008.

[99] Polymicro Technologies (http://www.polymicro.com/).

[100] Dow Corning (http://www.dowcorning.com/).

[101] C. M. Hessel, E. J. Henderson, and J. G. C. Veinot, "An investigation of the formation and growth of oxide-embedded silicon nanocrystals in hydrogen silsesquioxane-derived nanocomposites," *Journal of Physical Chemistry C*, vol. 111, no. 19, pp. 6956–6961, 2007.

[102] Fisher Scientific (http://www.fishersci.ca/) Product number: 3032515P01.

[103] Thermo Fisher Scientific. Density, refractive index and concentration data for sucrose at 20C, molecular weight = 342.3 (http://www.piramoon.com/sucrose.php).

[104] J. Rheims, J. Köser, and T. Wriedt, "Refractive-index measurements in the near-IR using an Abbe refractometer," *Measurement Science and Technology*, vol. 8, pp. 601–605, 1997.

[105] H. El-Kashef, "The necessary requirements imposed on polar dielectric laser dye solvents," *Physica B: Condensed Matter*, vol. 279, pp. 295–301, 2000.

[106] M. Daimon and A. Masumura, "Measurement of the refractive index of distilled water from the near-infrared region to the ultraviolet region," *Applied Optics*, vol. 46, pp. 3811–3820, 2007.

[107] Vector Labortatories Canada (https://www.vectorlabs.com) Biotinylated Bovine Serum Albumin (BSA), Product No. B-2007.

[108] Vector Labortatories Canada (https://www.vectorlabs.com) Streptavidin, Product No. SA-5000.

[109] N. Zammatteo, L. Jeanmart, S. Hamels, S. Courtois, P. Louette, L. Hevesi, and J. Remacle, "Comparison between different strategies of covalent attachement of DNA to glass surfaces to build DNA microarrays," *Analytical Biochemistry*, vol. 280, pp. 143–150, 2000.

[110] A. L. Stancik and E. B. Brauns, "A simple asymmetric lineshape for fitting infrared absorption spectra," *Vibrational Spectroscopy*, vol. 47, pp. 66–69, 2008.

[111] W. C. Karl and H. H. Pien, "High-resolution biosensor spectral peak shift estimation," *IEEE Transactions on Signal Processing*, vol. 53, pp. 4631–4639, 2005.

[112] G. H. Cross, A. A. Reeves, S. Brand, J. F. Popplewell, L. L. Peel, M. J. Swann, and N. J. Freeman, "A new quantitative optical biosensor for protein characterization," *Biosensors and Bioelectronics*, vol. 19, pp. 383–390, 2003.

[113] A. W. Poon, R. K. Chang, and J. A. Lock, "Spiral morphology-dependent resonances in an optical fiber: effects of fiber tilt and focused Gaussian beam illumination," *Optics Letters*, vol. 23, pp. 1105–1107, 1998.

[114] N. R. Lomb, "Least-squares frequency analysis of unequally spaced data," *Astrophysics and Space Science*, vol. 39, pp. 447–462, 1976.

[115] J. V. Herráez and R. Belda, "Refractive indices, densitites and excess molar volumes of monoalcohols + water," *Journal of Solution Chemistry*, vol. 35, no. 9, pp. 1315–1328, 2006.

[116] M. L. Korwin-Edson, A. G. Clare, M. M. Hall, and A. Goldstein, "Biospecificity of glass surfaces: streptavidin attachment to silica," in *Journal of Non-*

Crystalline Solids, vol. 349, pp. 260–266, Glass Science for High Technology, 16th Univeristy Conference on Glass Science, 2004.

[117] E. H. Williams, A. V. Davydov, A. Motayed, S. G. Sundaresan, P. Bocchini, L. J. Richter, G. Stan, K. Steffens, R. Zangmeister, J. A. Schreifels, and M. V. Rao, "Immobilization of streptavidin on 4H-SiC for biosensor development," *Applied Surface Science*, vol. 258, pp. 6056–6063, 2012.